Unconventional Approaches to Structured Semiconductors

Thesis by

Jonathan Ross Thompson

In Partial Fulfillment of the Requirements for

the degree of

Doctor of Philosophy

CALIFORNIA INSTITUTE OF TECHNOLOGY

Pasadena, California

2019

(Defended June 8th, 2018)

ACKNOWLEDGEMENTS

In my time in graduate school, I have had the indescribable pleasure of working with countless profoundly talented people. I specifically chose to delay writing the acknowledgments until I had completed the text of the thesis, thinking that this section should come easily. Now I realize that it is no mean feat to catalogue all the countless people who have made my time at Caltech better in one way or another over the last four and a half years. I apologize for any omissions in advance. Blame it on the fact that I am running on more coffee than sleep.

First, I need to thank my advisor Nate Lewis for the privilege of working in his group. He has given me an unbelievable amount of freedom to do the research I find interesting. I have enjoyed the research I have done the last few years in full recognition of the fact that having the intellectual freedom and access to resources afforded by Nate's mentorship is a once in a lifetime experience. But more importantly, I need to thank Nate for bringing me into his group and introducing me to all the exceptional people in his lab.

I would like to thank Professors Kathy Faber, Bill Johnson, and Harry Gray for serving on my committee. I am sure there are things you would all rather be doing at 3 pm on a Friday, and I appreciate that you were willing to help me with this.

Barbara Miralles has been a constant force of positivity, even as Noyes collapsed around all of us. She has never once been too busy to help me with any of my problems. Kimberly Papadantonakis, who has forgotten more about the subtleties of drafting email than I will ever know, has given me lots of valuable advice over the years, and I truly appreciate

all the help she has given me. Bruce Brunschwig has always been willing to offer advice or help fix equipment, even when he must have had other things that needed doing. He taught me that for every seven figure spectrometer there is a refurbished soda fountain pump keeping it running, and he is by far the most respectable person I have ever seen mutter curses under his breath at a cryo compressor.

Joseph Beardslee and Betar Gallant mentored me when I first joined the group, and I owe them both a debt of gratitude for that. They both spent a substantial amount of time showing me around the lab and helping me get started, which I deeply appreciate. More importantly, I thank them for all the helpful advice and guidance they provided me when I was an utterly lost new graduate student.

My fellow XPS GLAs have helped me in more ways that I can remember. Amanda Shing, Adam Nielander, and Noah Plymale showed me the ropes when I first took the job, and I appreciate their training and patience. I also need to thank the more recent GLAs Annelise Thompson, Ellen Yan, Michael Mazza, and Maureen Morla for trading off trainings, covering for me when I couldn't take care of something myself, and making what could be a stressful, time consuming job into an experience I will remember fondly.

I owe an enormous debt to my fellow graduate students who worked as part of the LMI-EFCR. Azhar Carim wears many hats; in any given day he will act as a chauffeur, a party planner, and a deliveryman, and he still somehow finds time to do science. On top of that, he integrated me into the group socially by sheer force of will. Ethan Simonoff, noted horse statuary and press cell connoisseur, has the remarkable ability and admirable tendency to enthusiastically help with any problem, big or small. He is also the only one who ever

stood up to Chris Wafer. Doing science by yourself is a horrible, lonely experience, and I owe so much to both of them, both for the invaluable help they have given me with my research and for making my time here much more rewarding. Sisir Yalamanchili was only in the LMI for a few months, but he stuck around for coffee once he was moved to a different grant, which is what really matters. Katie Hamann and Madeline Meier have made excellent additions to the group, both scientifically and socially. It's good to know that squigglers will keep squiggling, even after the weekly free pizza runs out.

I need to thank all off Noyes 220 for either putting up with or encouraging my idiocy. Back in the antediluvian days when we only had to worry about the lead dust raining down on us, the coffee breaks, paper clipping, and videos of animals making strange noises that we shared always brightened my day. I still hold dear to me a delirious breakfast we shared over gelatinous oatmeal.

I am not sure if I ever interacted with Fadl Saadi or Michael Lichterman scientifically, but I owe them both thanks for getting me to take advantage of living so close to Los Angeles. As it turns out, things get a lot more interesting once you are outside walking distance from Caltech. I'm happy that I had *the* original French dip (both of them!) before I left L.A., and I'm grateful for all the good times we shared not talking about science.

In addition to acknowledging all the people I regularly spent time with, I would also like to thank all the group members who I did not end up working with closely. I was going to list names, but I realized it would just be http://nsl.caltech.edu/home/people/ in list form. After I leave Caltech, I will remember all of you fondly. That is an astonishing statement for

a group of thirty some odd people, but it is absolutely true. You have all contributed in some way to making my graduate school experience what it was.

Ultimately, I owe everything to my family and the unflagging support they have given me. You supported me when I was the kid talking incessantly about cetaceans, and you still support me as the adult talking incessantly about butterfly wings. You have helped me get where I am in a thousand ways, both large and small, and any success I have, I owe in some way to you.

Finally, I want to acknowledge my wife Rachel for all that she has done for me. We met on campus my first semester at Caltech, we had our first lunch date over Ernie's in the BI courtyard, and we ultimately got married at the Athenaeum. My time at Caltech is inextricably tied to Rachel, and I would not have it any other way. The life of a graduate student is strange in countless ways, and having a partner who understands that is invaluable. Rachel has been supportive of me for years, and I thank her for all the help she has given me, be it advice, a sympathetic ear, or a well-timed cake to lift my spirits. I would not be where I am, or who I am, without Rachel.

ABSTRACT

The function of semiconductor devices is intrinsically tied to their structure. While there are already myriad techniques in use today to fabricate an extreme diversity of devices, new processes are regularly developed to make the production of previously unrealizable structures, and consequently devices, possible.

This dissertation deals with several unconventional approaches to generating ordered semiconductor structures. One chapter discusses a novel technique to measure the various forces that impede the alignment of randomly dispersed microstructures. The technique made it possible to both determine the magnitude of the interactions that the particles must overcome in order to be organized into a useful structure and assess the functional form of the forces that the microstructure is experiencing, thereby giving insight into the physical origin of said forces.

The following chapter deal with the spontaneous structure formation seen in photoelectrodeposited semiconductor films. One chapter investigates how the natural tendency of these films to form oriented, high aspect ratio structures can be coupled to the geometry of the substrate on which they are grown. This work demonstrates that extremely straight, high aspect ratio structures can be grown over macroscopic areas by making simple modifications of the substrate.

The final chapter characterizes the iridescence that these films exhibit. A simple physical explanation for the origin of the coloration is posited and verified. Then the information gleaned about the optical response of these films is used to generate vibrant, colorful patterns on electrode using consumer electronics.

TABLE OF CONTENTS

Chapter 1

INTRODUCTION

The consistent, microscopic structuring of materials influences, either directly or indirectly, every facet of modern life. This claim mostly rests on the ubiquity of integrated circuitry, accounting for over $400 billion in sales in 2017.[1] However, in addition to more familiar electronic devices, micromechanical electrical systems (MEMS) are present in as mundane of products as inkjet printer nozzles and tire pressure gauges.[2] The production of the structures that underlie the devices in these goods relies on many sophisticated processes, including photolithography, physical vapor deposition, chemical vapor deposition, and various etch methods, all of which come at astonishing cost.[3] In fact, the cost of a single state-of-the-art scanner (over $100,000,000)[4] exceeds the cost of a synchrotron light source.[5]

The cost of the commonly used commercial processes involved in structuring materials on the scale of tens of nanometers comes from several sources. Modern lithography employs exotic high power lights sources and extremely complicated optical systems to generate subwavelength features. Material deposition typically involves high vacuum chambers and expensive potentially hazardous precursor materials. Due to the nature of the devices being made, all materials involved need to be extremely pure. And because of the extreme sensitivity of all these processes, the commercial production of materials with sub-micron features must take place in costly dedicated facilities.

In contrast to these expensive and extremely precise pattering techniques are a host of alternatives that produce limited types of patterns, but at a small fraction of the cost of modern photolithography. For instance, techniques such as nanosphere lithography,[6] polymer buckling *via* solvent exposure or thermal treatment,[7] and anodic etching of silicon[8] all have been shown to generate micro- to nanoscopic patterns cheaply and facilely with minimal equipment requirements.

The work to be described in this thesis continues in the vein of the latter set of techniques. The following chapter delves into some of the practical concerns involved in generating structures from randomly distributed particles, particularly issues involving overcoming the adhesive force between the particles and other surfaces. The third chapter deals with the behavior of self-organizing electrodeposited semiconductor films in response to abrupt changes in substrate morphology, and how substrate modifications can be designed to influence the resulting film structure. Finally, the fourth chapter investigates the iridescence of highly ordered films such as those deposited in the previous chapter, with an eye towards their use as biomimetic coloration.

Chapter 2

DIRECT MEASUREMENT OF ADHESIVE FORCES PERTINENT TO THE ALIGNMENT OF RANDOMLY DISPERSED MICROWIRES

2.1 Introduction

Given the unabated year over year increases in energy consumption and atmospheric CO_2 concentration, finding sources of energy that do not contribute to global warming is one of the most pressing scientific and engineering challenges of our time.[9–13] However, the oftentimes tepid regulatory response to the threat of global warming points towards another requirement of any scientific solutions to the problem of energy production. It is not enough that solar energy generating devices be able to produce enough power to meet global demand; said devices must also do so economically enough that they can compete with fossil fuels with minimal governmental assistance.

Modifying the structure of the semiconductor used in solar energy harvesting devices can potentially improve the economics of green power generation. Controlling the structure of the semiconductors used in light absorbing devices is one of many techniques researchers have used to improve their devices' viability.[14–18] For instance, arrays of microscopic silicon cones have been shown to have greatly improved light absorption relative to planar silicon surfaces.[19] Improving light absorption improves both the voltage and current produced by a solar cell, resulting in substantial efficiency increase. Furthermore, structuring light absorbers can also improve the economics of solar energy generation by reducing the cost of

devices. A device geometry that improves light absorption efficiency also reduces the amount of material needed to absorb the light, thereby reducing the device cost. By decoupling the direction of light absorption and carrier collection, it also becomes possible to separate photogenerated electron-hole pairs without recombination while using worse light absorbing materials.[20]

However, for all the potential of structural control to improve the competitiveness of solar energy, one should keep in mind the crucial caveat that any structuring treatment can only be justified if the cost of the processing involved is outweighed by the improvement of the final device economics. Many syntheses of structured light absorbers are highly capital intensive processes, requiring some combination of high vacuum equipment, high temperature reactors, dangerous precursors, and lithographic patterning.[21,22] However, substantial effort has also been dedicated to the solution phase synthesis of semiconductors. The diversity of semiconductors synthesized *via* solution processes (perovskites, metal oxides, II-VI, and III-V materials)[23–28] exceeds the materials that can be deposited in CVD processes. These syntheses take place at moderate temperatures and pressures in standard laboratory glassware using relatively stable precursors. However, the resultant semiconductor particles lack the periodic structure necessary for most devices.

The self-assembly of nanoparticles has been well-studied, with reports of the assembly of varied structures, including face centered cubic and body centered cubic arrays and hexagonally close packed monolayers.[29–34] The spontaneous assembly of nanoparticles into ordered arrays relies on the small particle dimension. Due to the extremely small size of the particles under discussion, the inter-particle forces, which scale with surface area, can

overcome particle inertia, which scales with particle volume. However, larger particles have proven more troublesome to get to self-assemble, as the square-cube relationship between particle surface area and volume becomes less favorable with increased particle size. This fact proves troublesome, because some possible applications of oriented light absorbers would require semiconductor particles many microns across or larger, especially when indirect gap materials are used for the light absorbers. In the case of larger particles, external stimulus has proven helpful in effecting particle organization.

2.2 Background

Previously, researchers investigated using magnetic coatings to align randomly dispersed silicon microwires.[35] The motivation was several fold. First, the magnetic coating on the wires would give one a powerful handle with which the wire alignment could be controlled externally. Second, the nickel used in magnetic coatings would be multipurpose, potentially acting as an ohmic contact to silicon for device integration or as a catalyst in photoelectrochemical fuel generating device. Finally, in the case of the specific chemical vapor deposition grown microwires used for the study, the nickel coating was facilely applied using electrodeposition and the wires were shaved off the growth substrate, making possible the potential reuse of the relatively expensive growth wafers.

This study considered the alignment of the metal coated microwires in different solvents and off of different substrates. Wires were removed from the growth substrate, dispersed in isopropanol, drop cast onto the substrate of interest, and allowed to sit for the few minutes needed to let the isopropanol completely evaporate. The samples were then

placed in an electromagnet mounted to a microscope. The solvent, either deionized water or isopropanol, was then added to the sample, and the alignment of the wires *versus* applied magnetic field was monitored microscopically.

The experiments in this study showed that the different substrate-solvent combinations resulted in significantly different required field strengths to align over 90% of wires. Ranked from lowest required field to highest required field, the substrate-solvent pairings were hydrophilic silicon hydroxide (SiOH) and water, SiOH and isopropanol, and hydrophobic silicon hydride (SiH) and isopropanol. No appreciable alignment occurred for wires on SiH in water at the field strengths accessible with the experimental setup. However, while the relative strengths of solvent-dependent microwire-substrate interactions are accessible from these experiments, actual values for adhesion could not be measured. Since wire-substrate adhesion plays a central role in the alignment of randomly dispersed microwires, both in terms of allowing the wires to break free of the surface and limiting aggregation of wires at high wire loadings, there was interest in developing a technique that would let us directly measure the context-specific adhesion between wires and substrates, with an eye toward finding optimal conditions for alignment.

Force spectroscopy measurements have widely been used to collect adhesion data for standard atomic force microscope (AFM) tips, functionalized tips, and colloidal particles.[36–39] In these experiments, an AFM probe, consisting of a probe body that is mounted to the instrument, a thin reflective cantilever extending off of the probe body, and a tip on the underside of the cantilever, is lowered toward the surface of interest. As the tip comes into contact with the surface, the cantilever deflects upward or downward, to an extent dependent

on the strength of the interaction between the tip and the surface. Meanwhile, a laser beam is reflected off the back of the cantilever into a detector. As the cantilever deflects, the laser beam moves on the detector, which is then converted via calibration data into the upward or downward movement of the cantilever. Finally, given the spring constant of the cantilever, an application of Hooke's law coverts the cantilever deflection data into the force felt by the tip of the cantilever as a function of probe position. By noting the maximum force between the tip and the surface before the tip separates from the substrate, one measures the strength of adhesion between the tip and the surface.

2.3 Tip Preparation

These previous applications of the technique motivated using a similar approach to measure directly the adhesive force between microwires and various substrates. To accomplish this, custom AFM probes had to be prepared, but with nickel coated microwires in the place of the usual sharp tip. The wires were prepared as they were in the previous work on metal coated microwires. Silicon microwires were grown *via* chemical vapor deposition, giving 50 micron tall wires with diameters of 2 microns. Ohmic contact was made to the substrate by scratching a eutectic composition of GaIn (75% Ga, 25% In by weight) into the wafer. The wires' native oxide was removed with a buffered hydrofluoric acid etch, and the nickel was deposited potentiostatically at -1.0 V vs. Ag/AgCl for 10 minutes using a commercial nickel sulfamate based plating solution. The nickel plated wires were then shaved off the substrate and suspended in isopropanol. The wires were then drop cast onto a silicon wafer scrap, and the conformality of the coating was verified microscopically.

Wire-tipped AFM probes were prepared using tip free AFM probes (Bruker NP-O10). The tip free probes were mounted on a microscope slide using double sided tape. A wafer scrap with drop cast wires on it was mounted on the slide, and a small, roughly 1 mm diameter dot of epoxy (Hysol 9460) was added elsewhere to the slide. Using a very fine micromanipulator tip, a single wire was gently nudged until the wire broke free of the wafer scrap and adhered to the micromanipulator tip. The wire laden tip was then lifted away from the surface. A separate micromanipulator tip was used to collect a small amount of epoxy and spread the adhesive on the tip of the AFM cantilever. The wire on the tip was then set into the epoxy, and the epoxy was allowed to cure at room temperature overnight. The wire-tipped AFM probe was examined in a scanning electron microscope (SEM) to verify that the wire was properly seated and that the wire had not been damaged in the fabrication process, that the cantilever was in good condition, and that there was no adhesive on the bottom surface of the microwire.

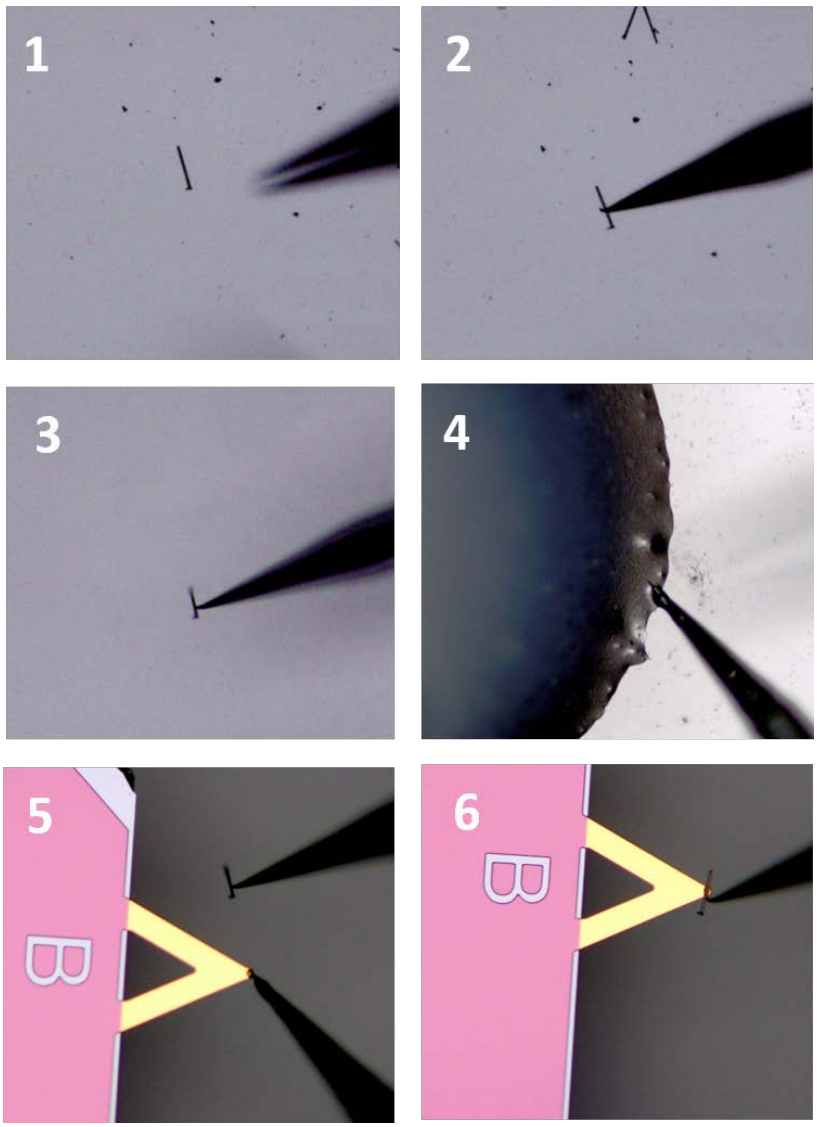

Figure 1: Fabrication of Custom AFM Tips

1) A metal coated wire on the substrate, 2) A micromanipulator tip pressed into the microwire, 3) The retracted micromanipulator tip with adhering wire, 4) A second micromanipulator tip collecting epoxy, 5) Application of epoxy to a tip free cantilever, and 6) Placing the microwire into the adhesive to fabricate the custom AFM tip

Once prepared, the effective spring constant of the custom AFM probes was measured using cantilever calibration standards (Bruker CLFC-NOBO). The deflector voltage-to-tip deflection conversion factor, or deflection sensitivity, was first measured by collecting deflection vs. probe extension data when extending the probe into a high hardness surface, in this case silicon. Applying the assumption that the silicon surface does not deform and that all the cantilever deflection is due to the tip deflecting upward, one can determine the calibration constant relating the measured detector voltage and the cantilever deflection. To then measure the cantilever spring constant, one then measures the apparent deflection sensitivity when pressing the wire into one of the calibration standards. Using the following equation,

$$k = k_{ref}\left(\frac{S_{ref}}{S_{hard}} - 1\right)\left(\frac{L}{L - \Delta L}\right)^3$$

the cantilever spring constant can then be determined for the custom AFM probe. Here k_{ref} is the spring constant of the reference cantilever, S_{ref} is the deflection sensitivity measured while in contact with the reference standard, S_{hard} is the deflection sensitivity against a hard surface, L is the reference cantilever length, and ΔL is the distance between the end of the reference cantilever and the point of contact with the AFM tip. Standard methods for determining the spring constant are unreliable for the custom probes because the addition of a relatively massive wire tip substantially changes the probe geometry from the typical case.

2.4 Adhesion Measurements

Adhesion measurements were first taken in air against both SiH and SiOH surfaces. Hydrophobic SiH surfaces were produces by dicing a degenerately doped ($\rho < 0.005\ \Omega\cdot$cm) n-type (111) silicon wafer (Addison Semiconductors) into 1 cm by 1 cm pieces, rinsing them with acetone, isopropanol, then water, and etching them in a buffered hydrofluoric acid solution (Transene) for 30 second. Hydrophilic SiOH surfaces were then prepared by subjecting freshly etched SiH surfaces to 10 minutes of UV-ozone cleaning. Contact angle measurements verified that the SiH surfaces were hydrophobic and the SiOH surfaces were hydrophilic. The adhesion measurements showed that the force of adhesion was similar for both the hydrophobic surface and the hydrophilic surface. This is attributed to the menisci that form in ambient environments, *i.e.* in the presence of even small amounts of water vapor in the air.[40,41] The surface tension in the menisci that form between the tip and the substrate appears to be far greater than whatever specific tip-substrate adhesion is present in each case. Experiments must be conducted in a liquid environment to measure adhesion without the conflating effects of water vapor.

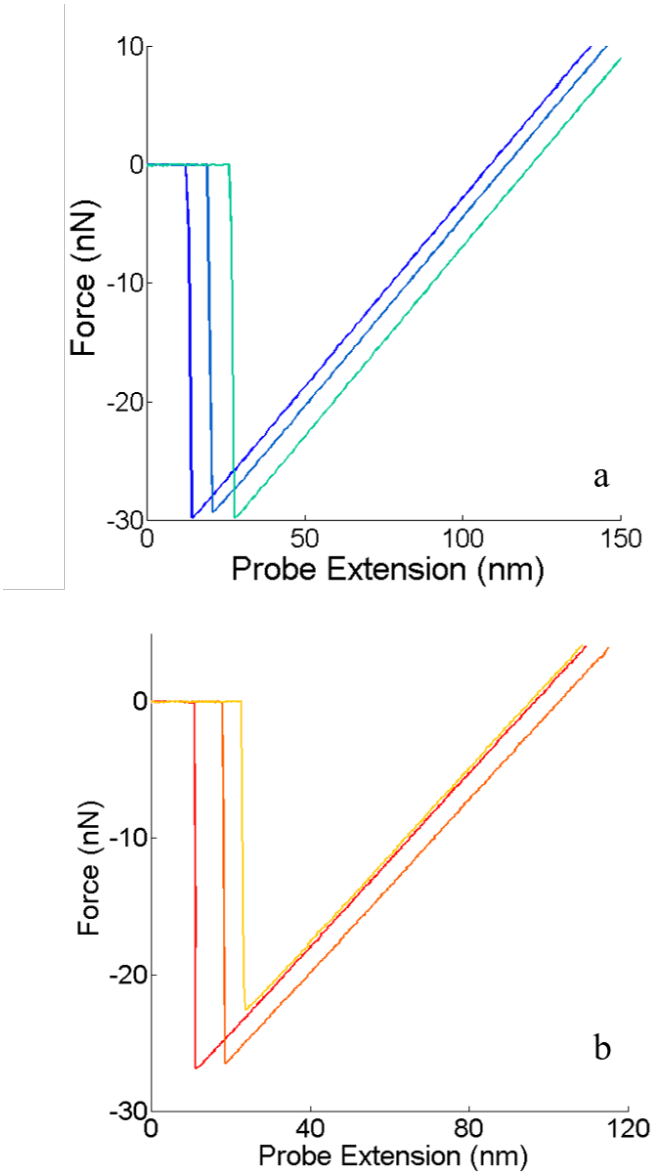

Figure 2: Force Curves taken in Air

(a) Repeated force curves taken versus a hydrophilic silicon dioxide surface in ambient air. (b) Force curves taken with the same tip versus a hydrophobic silicon hydride surface.

Measurements taken in 18 MΩ·cm deionized water freshly collected from a Barnstead Nanopure system showed that the adhesion between the hydrophobic SiH surface and the microwires is substantially higher than the adhesion between the SiOH surface and the microwires. This is in some ways an expected result; because the SiH surface is hydrophobic, the interface between the SiH and water is more energetically costly than the interface between the hydrophilic SiOH and water. Then it would follow that it should be more difficult to remove the wires from the hydrophobic surface in water than from the hydrophilic surface in water, because in pulling the wires off the surface, one is simultaneously generating the substrate-solvent interface everywhere the wire was previously in contact with the surface. The same measurements taken in isopropanol show minimal adhesion between the wires and either substrate. There is no discernible adhesion between the microwire and the SiOH substrate in isopropanol, and any apparent adhesion to the SiH surface is not clearly distinguishable from the baseline noise.

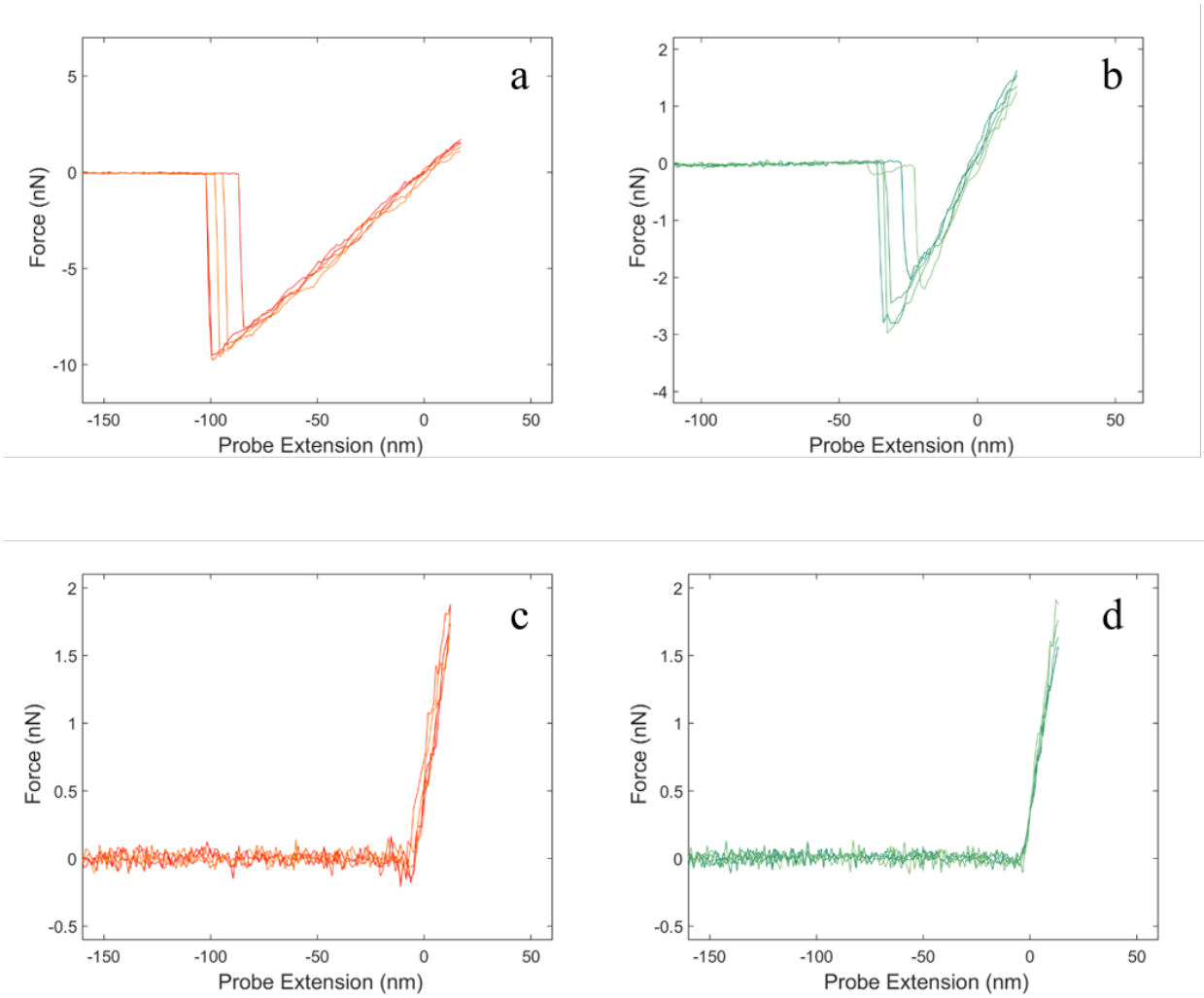

Figure 3: Force Curves taken in Water and Isopropanol

(a) Repeated force curves taken versus a hydrophobic silicon hydride surface in water. (b) Force curves taken versus a hydrophilic silicon hydroxide surface in water. (c) Force curves taken versus a hydrophobic silicon hydride surface in isopropanol. (d) Force curves taken versus a hydrophilic silicon hydroxide surface in isopropanol

These data are not consistent with alignment data from the previous study, assuming that the substrate-wire adhesion is the sole factor influencing alignment. From the magnetic alignment data alone, one would conclude that the relative adhesion strengths are Si-H/water > SiH/isopropanol > SiOH/isopropanol > SiOH/water. However, the actual forces of adhesion as measured *via* AFM are SiH/water > SiOH/water > SiH/isopropanol ≈ SiOH/water.

It is fruitful to consider the apparatuses in which these measurements are taken. In the case of the magnetic alignment, the substrate is placed in the center of an electromagnet made from coiled wire. The wire is insulated by encapsulating it in an insulating epoxy (Hysol 9460). By contrast, the AFM measurements previously discussed are performed in a cell with a metal base in electrical contact with the grounded chassis of the instrument. However, before the AFM measurement was refined completely, measurements were taken in a plastic petri dish instead of a dedicated, grounded cell. The force vs. distance curves occasionally featured a gradual detachment from the surface instead of the abrupt detachment expected from a tip overcoming adhesion force and coming free from the surface. This long range interaction is consistent with the length scale of coulombic interactions but not typical surface forces.

2.5 Coulombic Force Characterization

To further probe the nature of electrostatic forces in this system, adhesion measurements were performed in a solvent chosen to make the effects of the coulombic interaction as pronounced as possible. Hexane was chosen for this purpose because it is

sufficiently nonconductive to avoid dissipating built up charge, and it also has a small dipole moment so that the molecular dipole does not screen any charges present. The force-distance curves show very pronounced long range interaction, persisting even when the wire and the substrate are separated by hundreds of nanometers. Because the adhesion force is so strong and the probe has to be drawn roughly 100 nm away from the point of first contact between the wire and the substrate to get the wire to detach, the retraction curves lack data about the long distance interaction between the wire and the surface for separations less than 100 nm. Thankfully, the approach curves do have this information. By combining the probe extension data and the measured tip deflection, the force vs. probe extension data can be converted to force vs. wire-substrate separation.

The functional form of the force vs. separation can be better understood by plotting the data on log scale. There are two distinct regimes in this plot. First, at smaller separations, the force falls of like z^{-1}, where z is the separation between the wire and the substrate. At greater distances, the force begins falling like z^{-1}. This behavior is characteristic of the force felt by a charge in the electric field of a finite line charge:[42]

$$E = \frac{1}{4\pi\epsilon}\frac{2\lambda L}{z\sqrt{z^2 + L^2}}$$

where z is the distance between the test charge and the line charge, λ is the charge density, and L is the length of the line charge.

At separations much smaller than the length of the line charge, the finite line charge appears similar to an infinite line charge to the test charge, hence the z^{-1} behavior:

$$E = \frac{1}{4\pi\epsilon}\frac{2\lambda}{z}$$

At large distances, the line charge begins to appear more point-like, causing the electric field to vary like z^{-2}:

$$E = \frac{1}{4\pi\epsilon}\frac{2\lambda L}{z^2}$$

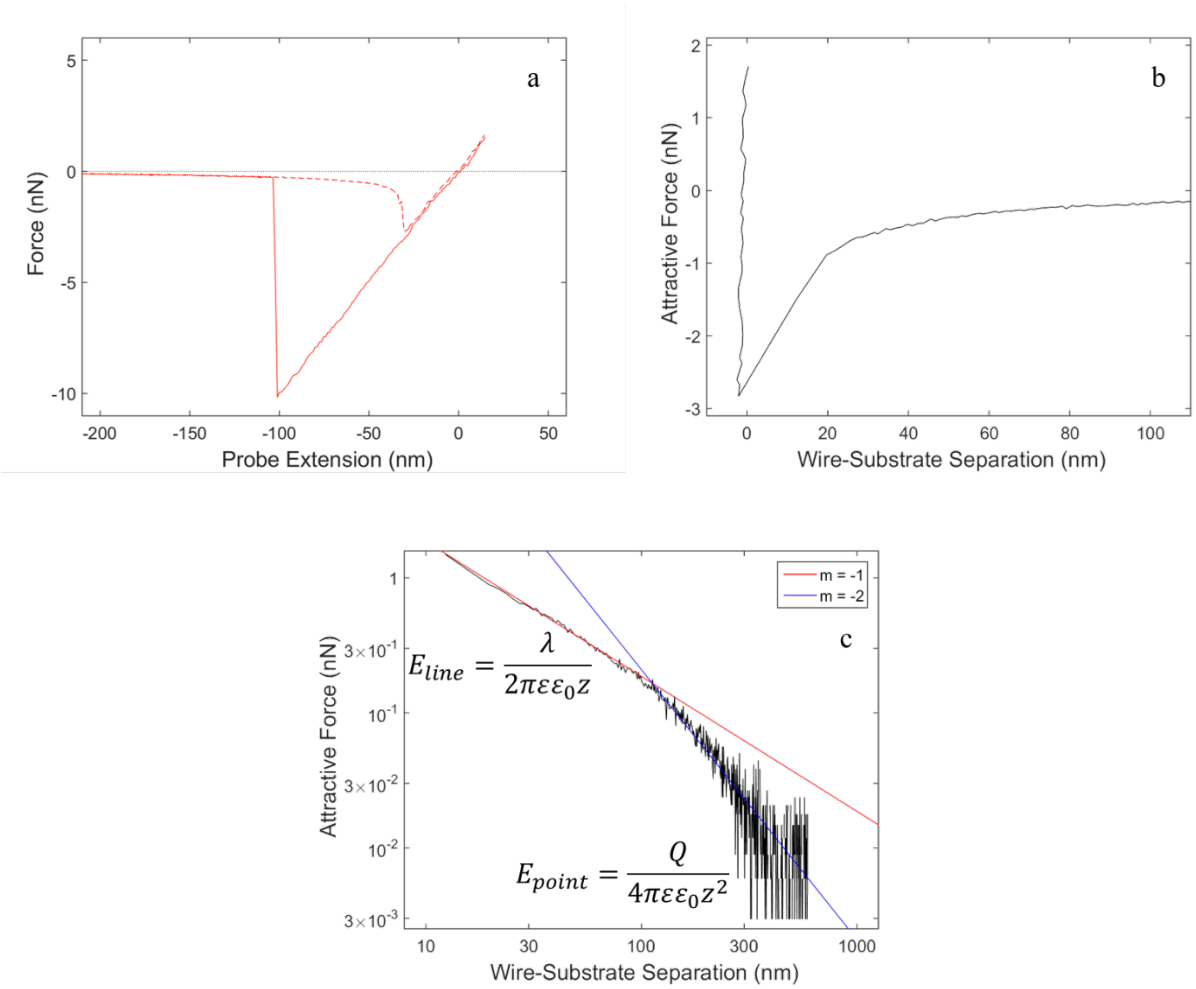

Figure 4: Analysis of Long Range Force

(a) Approach (dashed) and retraction (solid) force curves against silicon hydride in hexane. (b) Force versus wire-substrate separation for the approach curve. (c) Log-log plot of the force versus separation data

In reconciling this model with the physical system under investigation, we conclude that the line charges must be a feature of the wires. The substrates are all extremely flat, polished, and freshly cleaned silicon (111) surfaces. The wires, by contrast, have an electrodeposited nickel coating on them. The microwires' surface texture, including many linear domains, is apparent in scanning electron micrographs (SEMs). The charges that interact with the line charges are then concluded to be the image charges of the line charges generated in the highly conductive, degenerately doped silicon substrate.

With this model in hand, it becomes possible to extract useful physical information from the linear regions of the log-log plot of force vs. wire-substrate separation. The switch from one limiting regime to the other takes place at a wire-substrate separation of roughly 100 nm. This is consistent with the length of the raised linear regions visible in the texture of the metal coating. The linear charged domains appear to be the microscopic edges found on the nickel film.

The plausibility of this physical description of the long range interaction and the consistency with theory lend credibility to the argument that coulombic interactions can play a confounding role in the organization of micro- and nanoparticles. The AFM measurements performed in an insulating cell with isopropanol showed coulombic forces on the same order as the adhesive force of measured between the microwires and SiOH surfaces. The exact extent of charging that took place during the magnetic alignment measurements is indeterminate, depending on the electron affinity of the materials in the electromagnet encased cell, the trace water and ionic content of the isopropanol used, the material of the pipette used to dispense the solvent, and likely many other unaccounted for factors. However,

it can be said that the observed range of coulombic force magnitudes observed in isopropanol *via* AFM would be sufficient to explain the discrepancy between the relative difficulty of magnetically aligning randomly oriented nickel plated microwires in different contexts and the measured force of adhesion in those same conditions.

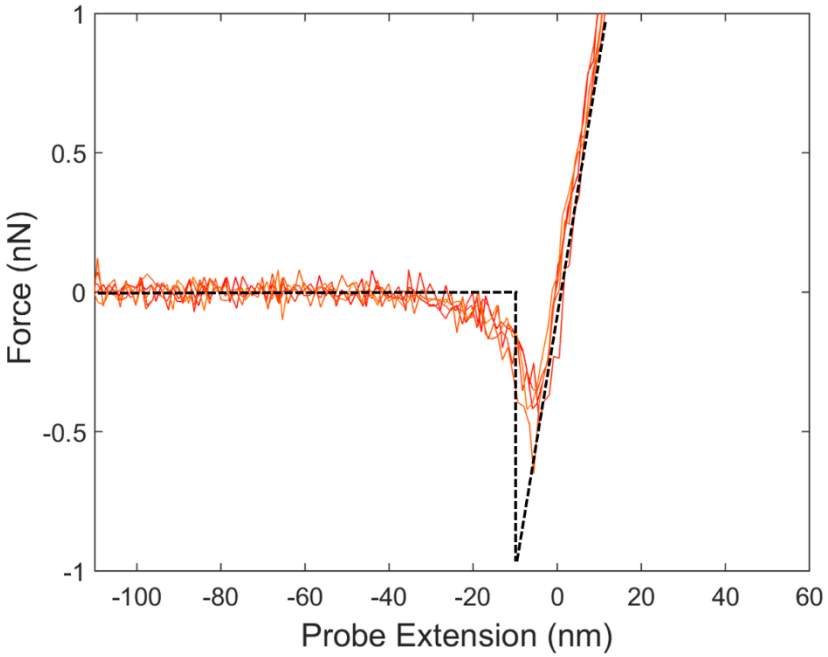

Figure 5: Evidence of Coulombic Force in Isopropanol

The force versus probe extension curve in isopropanol against a SiH surface. The black dashed line shows the expected curve shape in the absence of long range forces

2.6 Manipulating Adhesion with Surface Charge

Though the coulombic force observed in these measurements worked contrary to alignment, the strength of the attraction suggests that, if both the wires and the substrate were similarly charged, one could reduce the adhesive force, and possibly make the surfaces repel one another. Though there are many possible routes to generate surface charge, AFM measurements were used to characterize wires covalently functionalized with carboxylic acid moieties and wires that were charged electrochemically.

The silicon microwires to be chemically functionalized were grown in the same CVD process used to produce the wires that were then coated with nickel for the previous measurements. The wires were then functionalized using the procedure used by Gallant, *et. al.*[43] The adhesion between a silicon native oxide surface and the wires was measured in hydrochloric acid solutions from pH 1 to 6, in a neutral water solution, and in sodium hydroxide solutions from pH 8 to 13. The force curves at low pH were very similar to each other, as were the force curves at high pH, indicating that the solute concentration had minimal impact on the adhesion. However, in going from pH 5 to pH 6, the form of the adhesion curve changed qualitatively. In more acidic pH solutions, the curve had the familiar form showing adhesion between the wire and the substrate. At pH 6 and above, there was no measured adhesion. In fact, the force curve showed that the wire was repelled from the surface. Two physically relevant processes take place between pH 5 and 6. The pK_a of both surface-bound carboxylic acid groups and silicon hydroxide groups fall in that range.[44] As both surfaces go from neutral and protonated to negatively charged and deprotonated, the adhesion between the surfaces turns into repulsion. This effect illustrates that, by capitalizing

on the substrate and wire surface chemistry, it is possible to switch adhesion on and off in these systems using an easily controlled property such as solution pH.

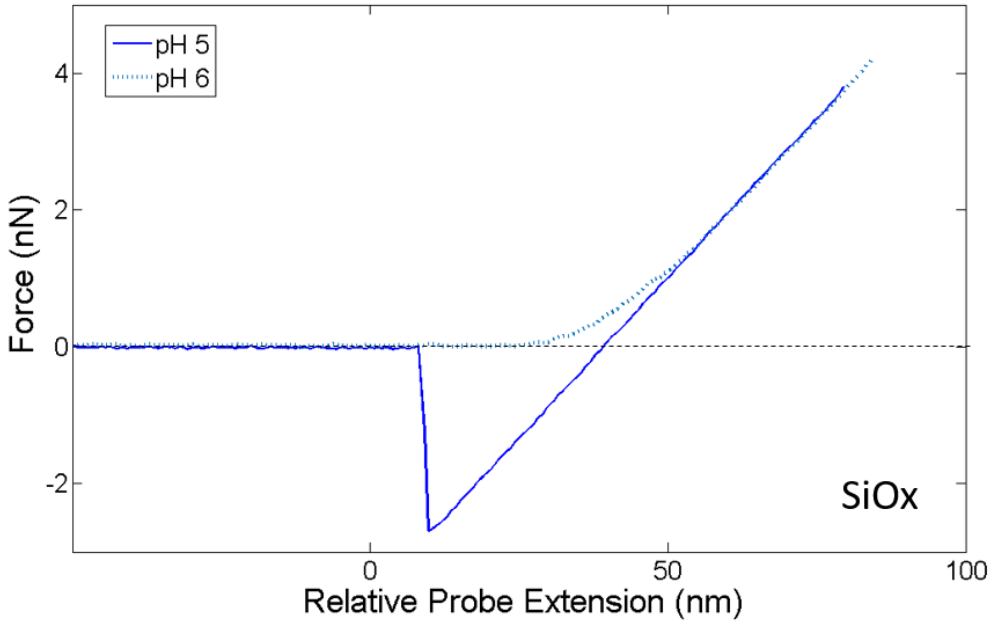

Figure 6: Wire-Substrate Adhesion at Varied pH

The retraction force curves for a carboxylic acid functionalized wire and a native silicon oxide surface in an aqueous HCl solution. The solid line was taken at pH 5 and the dashed lined at pH 6.

Motivated by the pH adhesion dependence, a more general method to tune adhesion was investigated using a redox couple in solution. The pH based adhesion modulation require there to be groups that can either be deprotonated or protonated on the surface of the wire and substrate. But there are many interesting physical systems where this is not the case. In the case of conductive materials, however, a redox couple can be used to control the charge of surfaces.[45] When a material is put in contact with a solution containing a redox couple at a potential different than the Fermi level of that material, charge will flow between the dissolved redox couple and the material until there is enough built up charge in the material and the electrochemical double layer to prevent further charge from passing. By modifying the solution potential, it should be possible to influence the charge on the surface of the material. In the following experiments, a nickel coated wire was used as the AFM tip and a silicon wafer piece sputter coated with gold was used as the substrate. Two solutions were used for the measurements. The control solution was a 1 M aqueous solution of potassium chloride, while the other solution was 1 M potassium chloride, 25 mM potassium ferricyanide, and 25 mM potassium ferrocyanide. The potential of the couple is higher than that of either metal, so both metal surfaces would be expected to be negatively charged in solution.[46] In the plots of force versus distance, the adhesion measured between the mutually charged surfaces is reduced to roughly one eighth of the adhesion measured in the control electrolyte solution. Though the preliminary experiments described here do not constitute a comprehensive investigation of the phenomena at play, they suggest the utility of solution potential as an easily adjusted control to influence adhesion between materials.

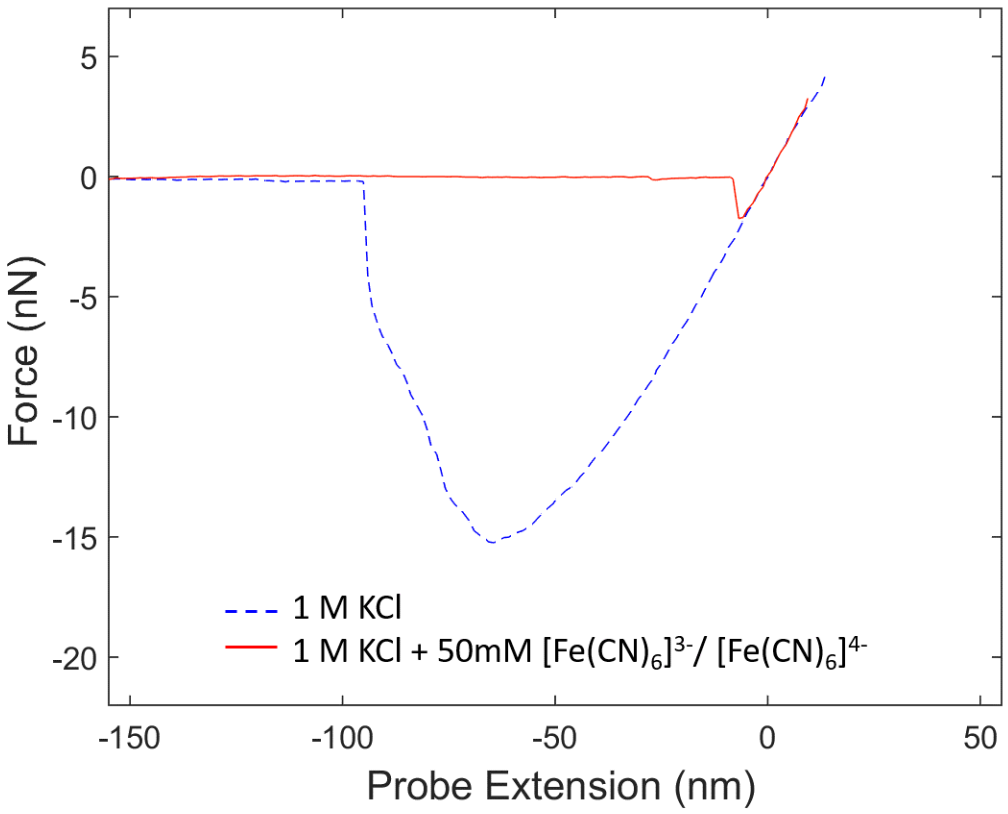

Figure 7: Redox Couple Dependent Adhesion

Force curves for a nickel coated wire in contact with a gold surface. The solid red line shows the data collected in the electrolyte control. The dashed blue line shows dramatically different behavior in the presence of the redox couple.

2.7 Conclusions

Force spectroscopy allowed the direct measurement of the interaction strength between metalized microwires and varied substrates. The AFM measurements made it possible to measure not only the strength of the interaction as a function of substrate surface chemistry and solvent environment, but also the dependence of the attractive force on wire-substrate separation. The measurement technique allowed the origin of the substrate-microwire interaction to be determined, which provided insights into how attempts to align randomly dispersed particles could be improved.

Chapter 3

THE INFLUENCE OF SUBSTRATE TEXTURE ON MORPHOLOGY OF SELF-STRUCTURING PHOTOELECTRODEPOSITED SEMICONDUCTOR FILMS

3.1 Introduction

There are many technologically significant methods for semiconductor structuring that are widely employed industrially. Photolithography and sophisticated etch processes have been employed for the fabrication of integrated circuits for decades.[47,48] There are also many selective wet chemical etch processes used in the production of strain sensors, pressure sensors, and myriad other micromachined devices.[49–52] Photoanodic etching can generate high aspect ratio structures by using electric fields internal to the material to direct the current that causes the material to undergo anodic etching.[53–56] These techniques produce well defined structures on large scales, though the cost is typically substantial.

While the cost of these processes depends on the expense of the equipment used to define the nanoscale features, ultimately all these processes will be limited by the fundamental costs of the materials being used. All the aforementioned processes are top down processes, where the structures are generated by the removal of material. In contrast, bottom up syntheses produce structures by adding material, so that the material cost closely tracks the cost of the material added. However, bottom up processes that rely on other expensive patterning processes will still be limited by the other processing steps; even a

cheap process, such as standard electrodeposition, will be limited in affordability if the areas where mass is being added are defined by some relatively expensive lithographic process.

3.2 Background

There is then value to processes that deposit mass in a self-structuring manner, ideally where the structuring is externally tunable. One such process is the photoelectrodeposition of chalcogenides reported by Sadtler, *et.al.*[57] The initial aim was to electrodeposit a semiconducting film containing selenium and tellurium. The deposition was conducted at moderate negative bias under illumination, with the aim of using the photovoltage generated by the deposited film to promote the further deposition of material. If the deposition of material is dependent on the photoactivity of the deposit, then any deposition conditions that produce substantial cathodic films will be likely to produce photoactive, p-type films. It was found that the morphology of the films generated in this manner depended on both the wavelength and polarization of the illumination.

In the case of unpolarized illumination, the resulting deposits had circular voids spread across the surface. However, when polarized light was used to illuminate the electrodes during deposition, lamellar ridges of a photoactive selenium tellurium alloy deposited aligned with the polarization direction of the light. The lateral spacing of the ridges deposited under polarized light was found to vary with the wavelength of the light used for the deposition. To first order the spacing between the ridges varies like $\lambda/2n$, where λ is the illumination wavelength and n is the refractive index of the solution in which the deposition

occurs. This suggested a mechanistic explanation involving interference of light scattered off the surface. The putative explanation was that randomly spaced dipole scatterers on the surface scattered light in the plane of the electrode surface. Multiple scatterers set up interference fringes on the surface, with a spacing between fringes given roughly approximately by $\lambda/2n$. Because light is a transverse electromagnetic wave, the oscillation of the dipole scatterers preferentially supports scattering normal to the polarization direction of the incident light. This explanation was born out by variable wavelength experiments, and the observed structure was recreated in optical simulations.

This result was both scientifically interesting and promising at a patterning technique. This simple, solution phase, mask free process was shown to generate relatively high fidelity sub wavelength features over macroscopic areas. In contrast to traditional lithography equipment, that can cost from hundreds of thousands to hundreds of millions of dollars, the only equipment needed for this spontaneous patterning process are a lamp, a polarizer, and a power supply. As an added benefit, the material deposited was necessarily of a sufficiently high quality to be photoactive.

Several papers followed this initial study, in which subsequent researchers varied the illumination conditions to influence the morphology of the deposited film. In one study, two separate light sources with the same polarization but different wavelengths were used in place of the single source used in the initial report of these structured films.[58] It was found that the period of the features in the resulting films was intermediate between the periods of films grown with either light source by itself. The final period was ultimately an intensity weighted average of the source wavelengths.

A separate investigation characterized the relationship between the relative polarizations and phases of two separate sources and the resulting films.[59] Circularly polarized light and unpolarized light generated similar mesh-like structures, with pores in the film spaced isotropically throughout the deposit. When elliptically polarized light was instead used, the morphology of the deposits was intermediate between the linear, highly ordered growths formed from linearly polarized light and the structurally disordered mesh like pores characteristic of films grown using unpolarized light, with more linear growth apparent along the major axis of the ellipse and a level of disorder related to the eccentricity of the polarization of the light.

Furthermore, an investigation into electrodepositing films using two sources of different wavelengths with orthogonal polarizations found that said experimental conditions produced two sets of crossed, perpendicular lamella, each with periods and orientations dictated by the relevant light source's wavelength and polarization.[60] The relative heights of the two sets of lamellar depended on the intensity of the light used for growth.

The generation of structured films during illuminated electrodeposition of semiconductors was shown to be generalizable beyond the selenium tellurium system used in the previous studies, as well. Lead selenide films were deposited under similar conditions to those used for the selenium tellurium films, and lamellar structures were observed in the resulting films.[61]

These studies all featured computational modeling as a complement to experimental results. The model was a two-step process, where first light absorption was modeled using a

commercial software package (Lumerical FDTD Solutions), and then material was added to the simulated structure dependent on the intensity of local carrier generation. This process was iterated to simulate the feedback-induced structuring that takes place during electrodeposition. The simulations successfully reproduced the experimental results, using only the material's complex refractive index, carrier lifetime, and electron mobility as inputs. This suggests that the spontaneous growth of these structures is principally governed by the light scattering that takes within the deposit, not by the electrochemistry involved in the plating.

Taken together, these previous works elucidate how varied optical inputs can serve as a powerful handle with which to manipulate the morphology of these electrodeposited films. However, the illumination used for a deposition is only one part of the light scattering that takes place on the surface of photoelectrodes. The surface itself also influences the sort of scattering that can occur. On a highly planar, polished silicon electrode, as was used in the previous studies, the origin of the light scattering particles was taken to be the disordered deposition of non-photoactive material prior to the photoelectrodeposition taking over at later times. There was interest in understanding the effect on film morphology of anisotropic distributions of scatterers.

Part of this interest derived from the lack of straightness in the lamellar growths that form on planar substrates. Some of the disorder that appears in these structured films can be attributed to the initial disorder in the random dark growth at the start of the process. As shown in the schematic below, while the scatterers that are offset by a vector normal to the incident light's polarization vector contribute strongly to growth perpendicular to the

polarization axis, diagonally oriented scatterer pairs also produce interference fringes that promote the deposition of material. Furthermore, even assuming scattering only takes place between scattering pairs oriented perpendicularly to the polarization direction of the light, with random nucleation of scattering pairs, there will inevitably be regions that are not in registry with one another. When these misaligned regions grow together, there will necessarily be mismatch at the interface between the different domains. Additionally, the interaction between these self-ordering growths and features on the growth substrate warrants investigation because if these structures are to be of any interest industrially, they must be able to be directed to grow at a specific location on a substrate in order to use them in device fabrication.

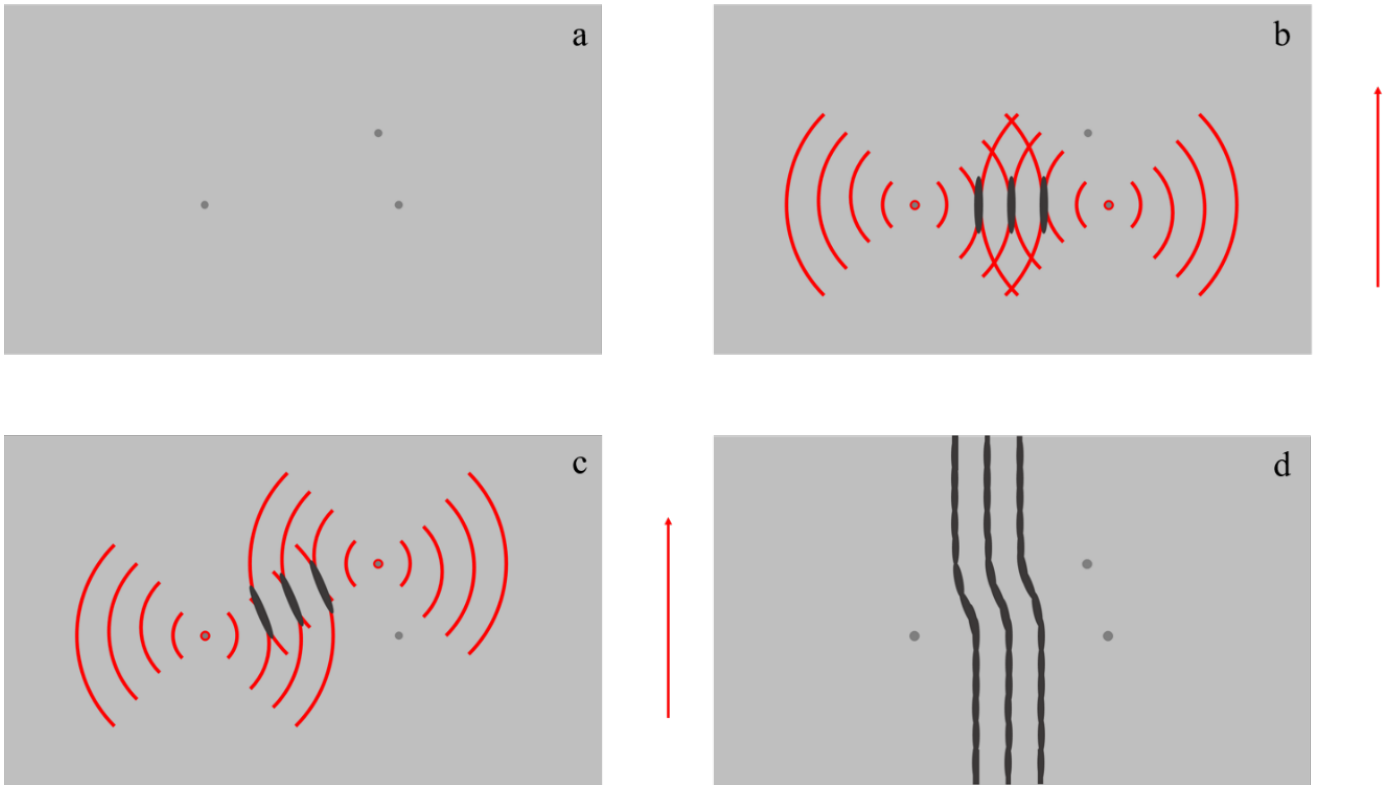

Figure 8: Mechanism for Formation of Kinked Lamellae

(a) A hypothetical surface containing three scattering particles. (b) Vertically polarized light scattering off the horizontally oriented particles. Interference maxima cause localized deposition of material. (c) Vertically polarized light scattering off diagonally oriented particles. As before, material is deposited at regions of constructive interference. (d) An extrapolation of the lamellar structure that would develop from this distribution of particles. The otherwise straight lamellae kink due to the random distribution of particles.

3.3 Ordered Growth on Abraded Electrodes

Insight into the role of surface texture on film morphology was serendipitously gleaned during investigations into growing lamella on materials other than silicon. Platinum surface electrodes were fabricated by etching a (111) single side polished silicon wafer (Addison Wafers, n type, P doped, $\rho < 0.005\ \Omega\cdot cm$) in buffered hydrofluoric acid (Transene) for 30 seconds to remove surface oxide. The wafer was then loaded into a metal evaporator (Denton Vacuum) and pumped down to less than $1\cdot10^{-5}$ Torr. A 10 nm layer of titanium (Kurt J. Lesker Company, 99.995%) was deposited *via* electron beam evaporation at 10 kV accelerating voltage and 40 mA emission current. This layer formed an ohmic contact to the silicon as well as serving as an adhesion layer. A 50 nm platinum layer (Kurt J. Lesker Company, 99.99%) was subsequently deposited on the titanium layer without breaking vacuum. The wafer was then scribed into squares approximately 5 mm on a side. A eutectic composition of gallium (Alfa Aesar, 99.99%) and indium (Kurt J. Lesker Company, 99.99%) was scratched into the back side of the electrodes to make ohmic contact. Electrodes were then fixed to aluminum rods with flash dry silver conductive paint (SPI Supplies), and the edges of the electrodes and any exposed metal were covered with clear nitrocellulose-based nail polish.

Photoelectrodeposition was performed potentiostatically at -0.2 V vs Ag/AgCl (CH Instruments, 1 M KCl solution) for 150.0 seconds using a Bio-Logic VMP-3 multichannel potentiostat. The plating bath was an aqueous solution composed of 20.0 mM SeO_2 (Alfa

Aesar, 99.5%), 10.0 mM TeO_2 (Sigma Aldrich, 99%) and 2.00 M H_2SO_4 (J. T. Baker. ACS Reagent Grade). A 6 mm diameter graphite rod (Sigma Aldrich, 99.995%) was used as the counter electrode. Samples were illuminated with a broad spectrum halogen lamp fitted with an ELH bulb. The light was directed through a glass diffuser (Thorlabs, DG20-600) before being passed through a wire grid polarizer (Edmund Optics, #34-254) into the electrochemical cell. A photodiode (Thorlabs, FDS100) inserted into the electrochemical cell was used to measure light intensity. The intensity was tuned to 25 $mW \cdot cm^{-2}$ by adjusting the positions of the lamp and the polarizer.

Following deposition, electrodes were examined in a scanning electron microscope. It was observed that, while most of the surface exhibited the sort of morphology seen in previous studies, there were many isolated domains of abnormally straight lamellar growth. Besides being morphologically distinct from the surrounding area, the orientation of the straight lamella often differed from the orientation of the rest of the film's lamella. Instead of growing along the polarization direction of the light, the straight lamella would often grow several degrees rotated from the expected direction, though no large regions of straight growth were observed offset more than 15° from the polarization direction. Interesting features were also growing at larger angles from the polarization directions. At offsets between 15° and 50°, lines of doglegs in the lamella were observed. The lamella on one side of the feature would briefly grow at a different angle at the feature, before returning to the normal growth direction on the other side of the feature. At higher angles than that, the underlying structure produced abrupt breaks in the lamellar growths.

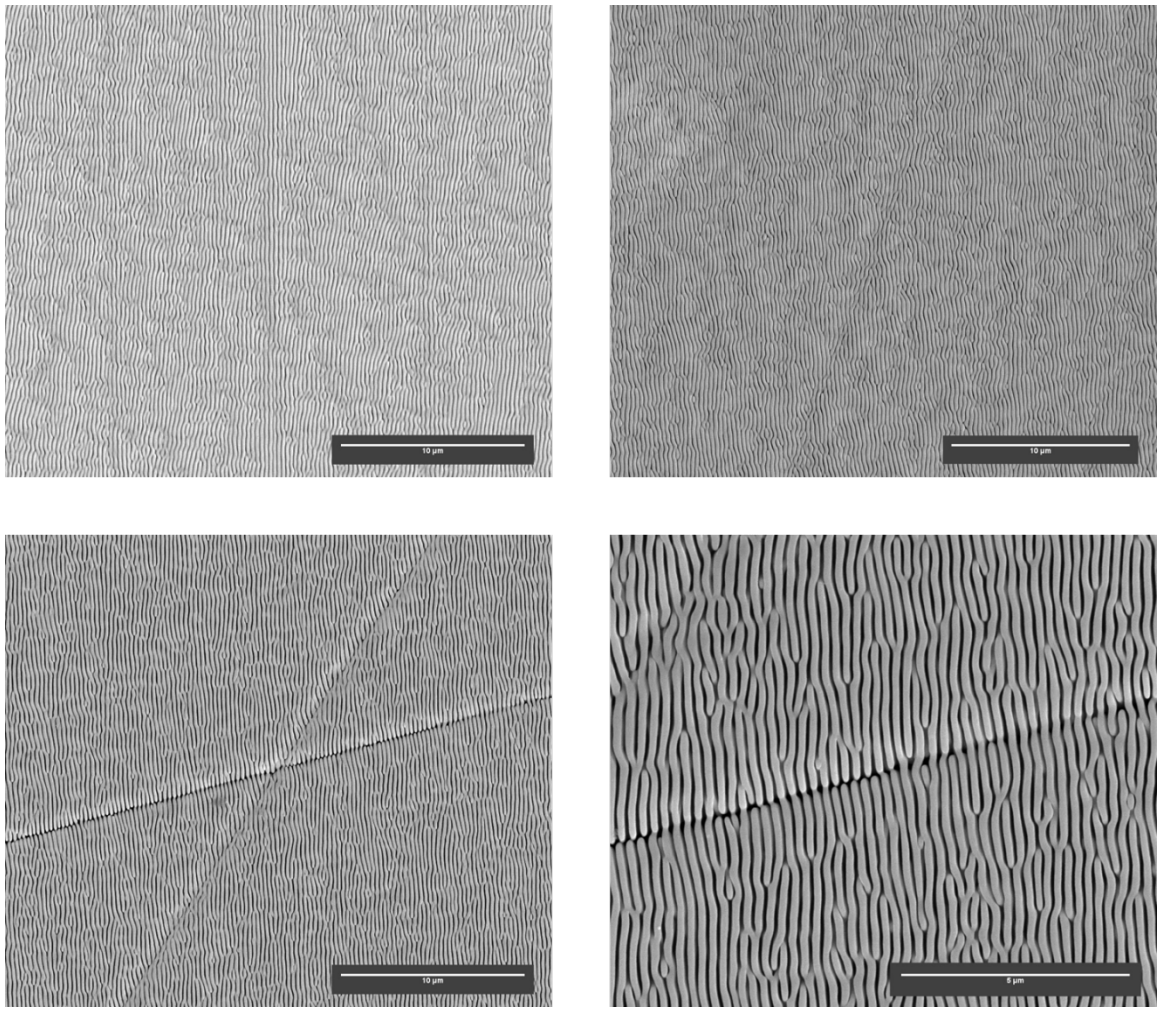

Figure 9: Lamellar Morphology near Scratches

Top left: Domains of abnormally straight growth slightly misaligned with overall lamellar growth. Top right: Diagonal “dogleg” pattern that appears when underlying structure is misaligned with polarization direction. Bottom left: Overview of growth near deep, crossed scratches. Bottom right: higher magnification of the features in the bottom left image.

These domains of distinct growth have only been observed on metalized silicon surfaces, never on uncoated silicon electrodes. The random orientation of the straight domains and their presence only on surfaces that have a deformable top layer informed the hypothesis that the ordered domains were a consequence of scratches made inadvertently during the electrode fabrication process. When the GaIn eutectic was scratched into the back of the electrodes, the faces of the electrodes may have been abraded by the clean room wipes (Texwipe, TX624) they were placed. Silicon, by contrast, is substantially harder than platinum, and would be less likely to pick up scratches in this process.

These scratches could be a source for the nonrandom scatterers needed to impose greater order on the deposited films. The ridges created accidentally during handling could be good light scatterers themselves. It is also possible that the abrasions could serve as nucleation centers for the selenium tellurium alloy, which could then serve as a dipole scatterer itself.

3.4 Simulated Growth

Simulations were done to explore the role of ridges in controlling the lamellar structure of films grown on nonplanar substrates. The simulations involved a two-step process to simulate light absorption in the computed structure and add material to regions with the highest list absorption. The growth in the vicinity of a single 100 nm wide by 100 nm tall ridge was simulated using 630 nm incident light polarized such that the polarization vector ran parallel to the ridge. It should be noted that the boundary conditions for these simulations are periodic, so the nominally isolated ridge is in fact physically analogous to an

array of ridges spaced 6 microns from one another. However, as the simulation results will indicate, the effects of the ridge are short ranged enough that any effects due to long range periodicity can be discounted.

The grayscale images are simulated scanning electron micrographs. They are generated by taking the three dimensional simulated volumes and determining the highest voxel occupied in each column. A shade of gray is then assigned to each coordinate, with a white pixel assigned to the highest maximal cell in each simulation iteration and a black cell assigned to the lowest maximal cell. This generates images that look similar to SEMs taken with correctly adjusted brightness and contrast.

In the control simulations, the early iterations result in the addition of matter randomly across the surface. This is a consequence of the fact that matter addition in the model is weighted by the local light absorption, but it is still added randomly. At early times, light absorption is equal throughout the surface, so the matter is added isotropically. In later iterations, there are subtle ridges that are just becoming visible. As some regions randomly gain matter in a configuration conducive to lateral scattering, the light absorption in those regions becomes anisotropic, resulting in the deposition of these early ridges. The emergence of the lamella progresses further in subsequent iterations. The apparent roughness decreases as the height of the lamella becomes much greater than the height of the random surface roughness. Finally, in the last shown iteration, the simulation arrives at a structure very similar to the result one would actually arrive at by electrodepositing the selenium tellurium alloy under illumination.

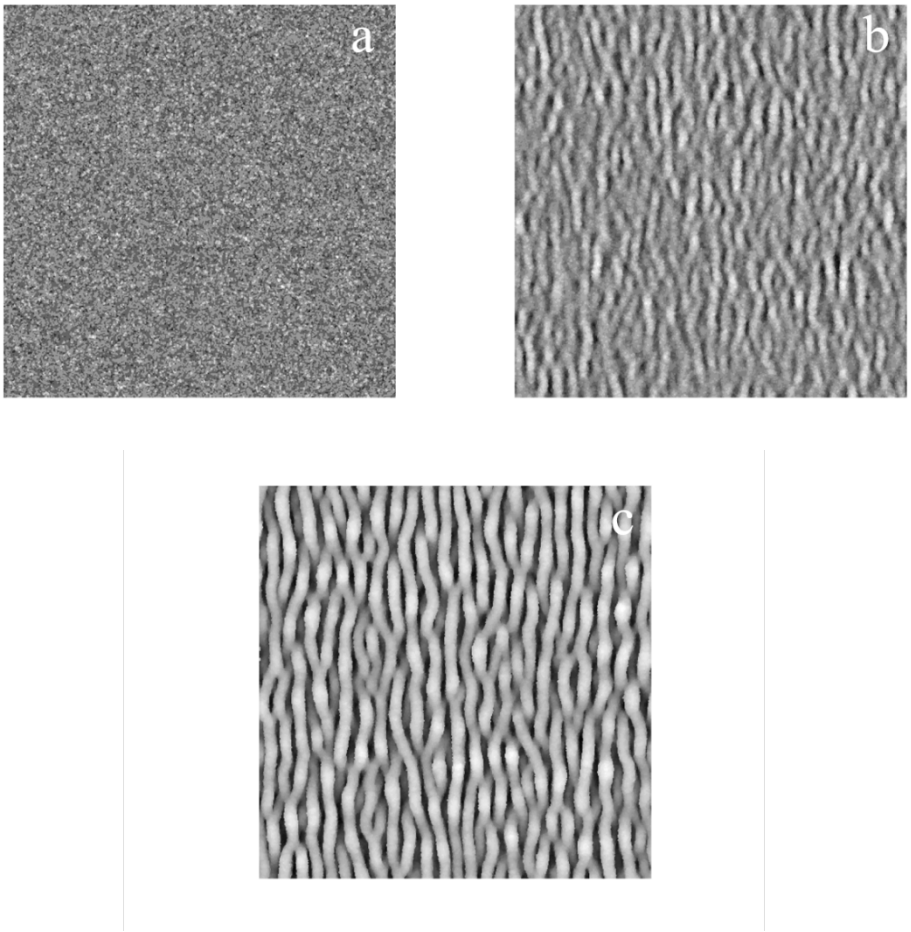

Figure 10: Simulated Growth on a Planar Surface

(a) Early simulation iteration showing only random nucleation on the surface. (b) Intermediate iteration highlighting the early development of lamellar features. (c) Final iteration, with fully developed lamellae throughout the simulation area.

In the earliest iterations of the simulation with the substrate with a single ridge, the deposition in the planar portion of the substrate also appears to be isotropic. This is the expected result. The platinum substrate is not photoactive, so the model does not weight the light absorption in the addition of mass. A photoactive layer of the selenium tellurium alloy must first be deposited to generate light mediated growth. Later iterations show precisely this happening. Once the randomly added selenium tellurium layer is in place, light absorption becomes highly localized in bands adjacent to the scattering ridge. The bands directly adjacent to the ridge are the most pronounced, but a second set of band further from the ridge are just visible. Subsequent iterations show the formation of relatively long, continuous lamella where the innermost bands were in the previous iterations. These lamella are not as straight at the central ridge, but they are much straighter than the surrounding lamella growing in the planar region. The growth on the top of the ridge is also bifurcating and spreading outward into the space nearby. This is likely caused by the strong absorption at the edges of the ridge directing growth to the ridge's corners and sidewalls. The two lamella that develop on the top of the ridge seem to effectively crowd one another out of the center of the ridge. This is likely the result of the developing lamella absorbing the light that would otherwise reach the center of the ridge and make possible the growth needed to bridge the gap between the two ridge lamella. In the final iteration, two extremely straight lamella have been formed from the central ridge. The lamella immediately adjacent to the central ridge are appreciably straighter than lamella from the control simulations, as well. As lamella get further from the ridge, however, they revert to a level of disorder that almost matches the disorder of the control case. This can be rationalized by considering the scatterer distribution argument previously put forward. The lamella immediately adjacent to the ridge have

randomly distributed scatterers on one side, and a continuous line of scatterers on the other. This can be credited with the increased straightness of the lamella next to the ridge as opposed to the control lamella. However, while they are straighter than they would be without the influence of the ridge, the straightened lamella are not as straight as the ridge. The second lamella out from the ridge are principally influenced in their growth by the random scatterers in the planar region on one side and by the abnormally straight, but still not perfectly straight, growths that form adjacent to the ridge. Lamella even further from the ridge are increasingly disordered as they get further from the ridge, until they are ultimately not appreciably more ordered than the lamella observed in the control simulation.

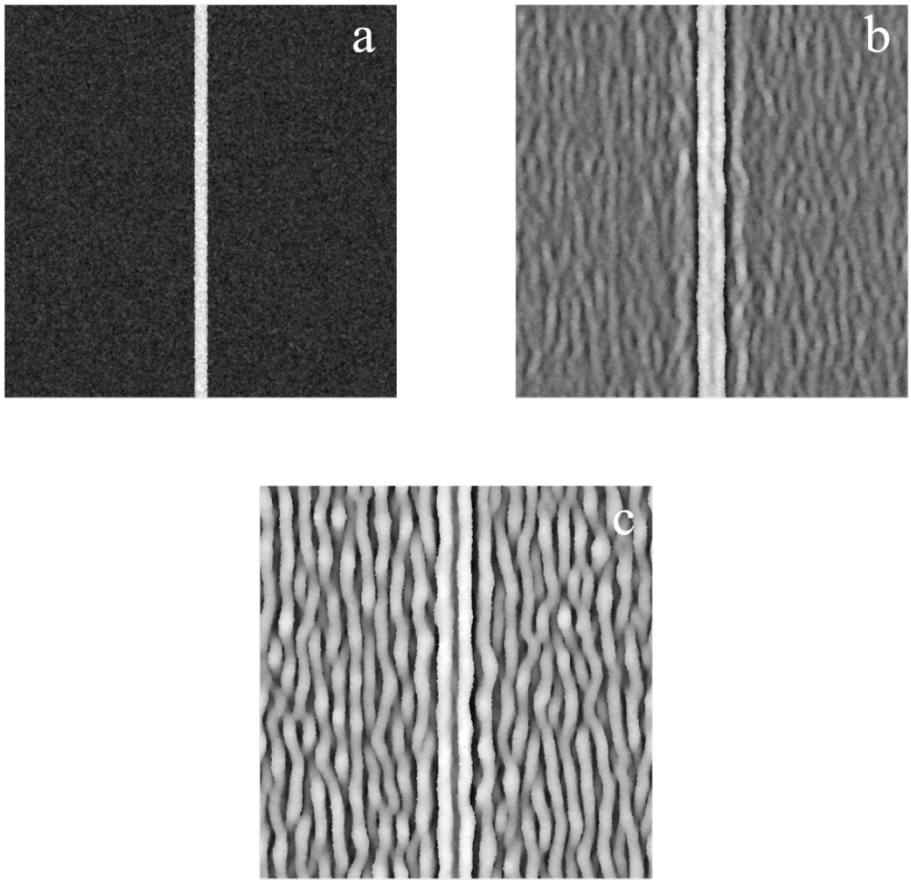

Figure 11: Simulated Film Morphology at a Ridge

(a) Initial simulation iteration showing the narrow ridge as the dominant feature on the electrode. (b) Intermediate image showing the film morphology developing in response to the substrate structure. (c) Final iteration illustrating the straight lamellar growth predicted in the vicinity of the ridge.

The previously discussed simulation offered insight into the growth near a ridge, but that is not the only geometry that might be generated by a scratch in a surface. Abrasions would also create abrupt edges where the surface of the material transitions from the cavity generated by the scratch to the original surface level. To understand the behavior at these step edges, a simulation was performed under the same conditions as before, except with a substrate featuring a 100 nm tall, 3 μm wide strip of material rising out of the electrode surface. At early times, the growth, as before, is isotropic since there is insufficient photoactive material deposited on the substrate to generate anisotropic light absorption. Shortly thereafter, straightened lamella develop adjacent to the step edges. These bands occur on both the upper and the lower surfaces. The lamella that grow right on the edges of the ridge are extremely straight, and they appear to expand outward into the space above the lower region. These lamella grow outward, likely because the outside edges of the step edge lamella absorb more light than the inner edges. The inner edges are effectively competing with the material in the adjacent lamella for light, while the outer edges have no such nearby competition, causing more light to be absorb on those edges, which in turn promotes the outward growth of the step edge lamella. As before, the ordering generated by the modified substrate geometry does not strongly influence the deposited film morphology more than one lamella away from the step edge.

The short range effect of surface perturbations on lamellar ordering suggests that the patches of the platinized electrodes that exhibit extraordinary straightness may be the result of many parallel grooves on the order of the wavelength of light. This possibility was also investigated *via* simulation. A series of simulations were conducted with substrates with

multiple parallel 100 nm by 100 nm ridges. The simulated electrode area was 6 μm by 6 μm. Simulations were conducted with four ridges per substrate with a ridge-to-ridge pitch of 1.5 μm, eight ridges with a 750 nm pitch, sixteen ridges with a 375 nm pitch, and thirty two ridges pitched 187.5 nm apart.

The simulation featuring the most widely spaced ridges resulted in straightened growth across the entire substrate. The ridges gave rise to the straightest lamella, as seen previously. The lamella that formed adjacent to the ridges were straighter than the nearest neighbor lamella that grew adjacent to the step edges or the isolated ridges. In those two cases, the disorder in the lamella adjacent to the ridge was attributed to the random distribution of scattering sites on the side of the lamella opposite to the substrate feature. In the case of closely packed ridges, this same argument no longer applies. Instead of having randomly placed scatterers, the lamella adjacent to the ridges have other ridge-adjacent lamella as the source of the light scattering from the side opposite the ridge. Notably, none of the lamellar branching at the top of the ridges that took place in the isolated ridge simulation was observed in this experiment. In contrast to the isolated ridge case, where there was enough disordered growth to allow the lamella adjacent to bow outward and make room for the ridge lamella to widen and ultimately split, the multiple ridge case has built-in geometrical constraints on how far a lamella can move before it gets too close to another lamella to absorb enough light to continue growing. The packing of the straightened lamella forces the ridge lamella not to split. Counting from left to right and accounting for periodic boundary conditions, there are twelve lamella in 6 μm, for a lamella-to-lamella pitch of 500 nm. The expected pitch for a planar substrate is 235 nm. When deposition takes place on a

randomly nucleated surface, there will in general be some scattering sites spaced the expected $\lambda/2n$ apart. In the structured case, however, the scattering is dominated by the ridges, which may explain the approximate pitch doubling observed in this simulation.

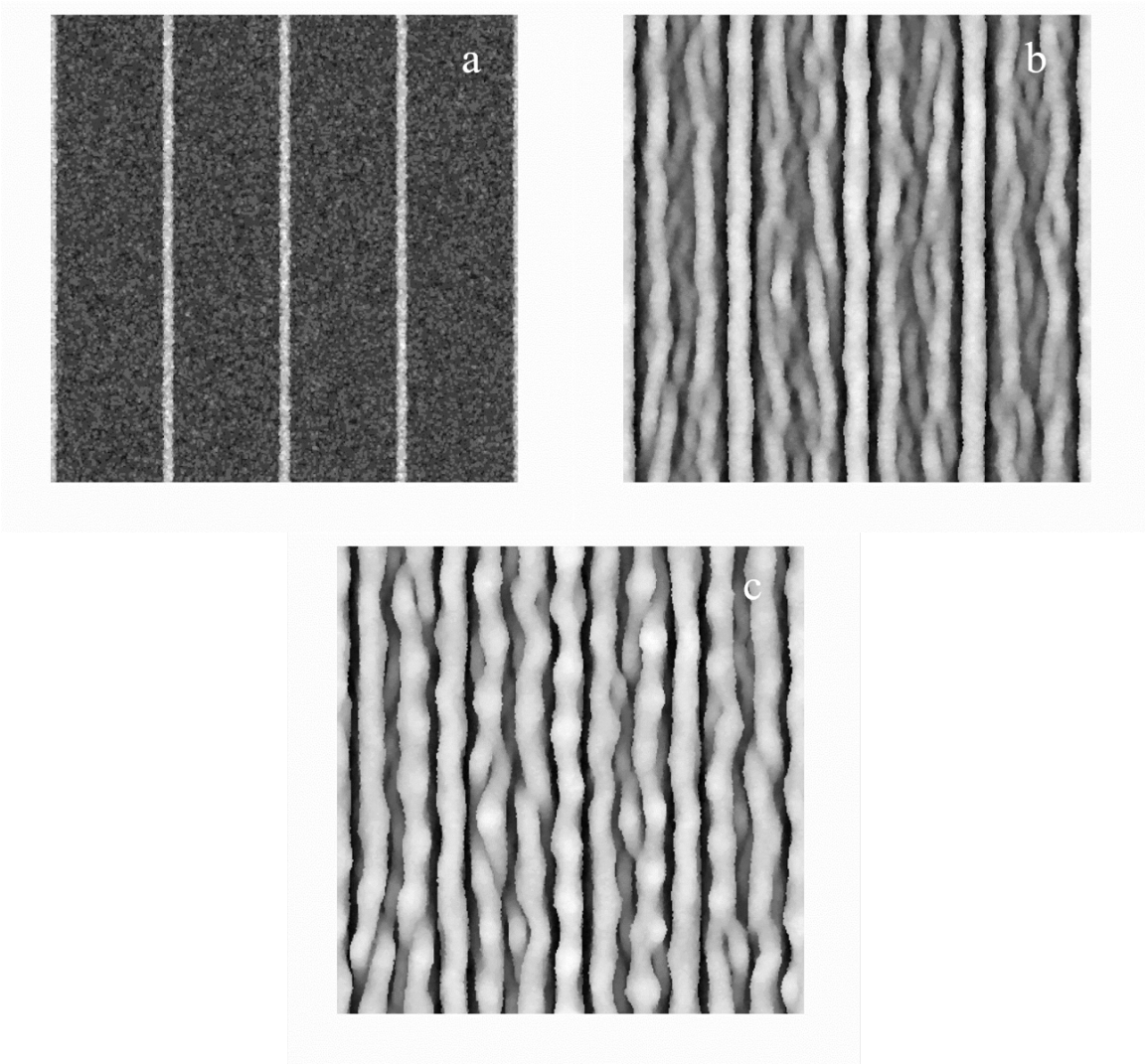

Figure 12: Simulated Film Morphology near 1.5 Micron Pitch Ridges

(a) Initial simulation iteration showing the narrow ridges as the dominant features on the electrode. (b) Intermediate image showing the film morphology developing in response to the substrate structure. (c) Final iteration illustrating growth straighter than the control throughout the sample.

The next simulation in the set is the simulation with ridges spaced 750 nm apart. Early growth between the ridges is spread throughout the available area, with the notable lack of growth immediately adjacent to the ridges. This is in fact a general feature of these simulations. The ridges effectively get the first chance to absorb the incoming light, and they are able to absorb light that would otherwise reach the surface near the edge. This is why there is so little growth immediately adjacent to the ridges. As the structure develops, the growth between any given pair of ridges converges to a single lamella. These lamellar are as straight as the ridge derived lamella. The lamella that grow on the flat substrate have ridge derived scatterers on both sides of them. In this case, there is minimal disorder among the scatterers that direct the growth of the substrate lamella, so these lamella become very straight. Once again there is a discrepancy between the predicted pitch for growth on planar substrates and the growth seen in this simulation. Here the measured pitch is 375 nm, compared to the prediction of 235 nm and the previous observation of 500 nm. Early iterations is this simulation show that there is initially a wide band where light is being scattered, as indicated by where the matter is deposited. However, as seen in the previous simulation, the growth converges to a structure that depends on the initial geometry of the substrate.

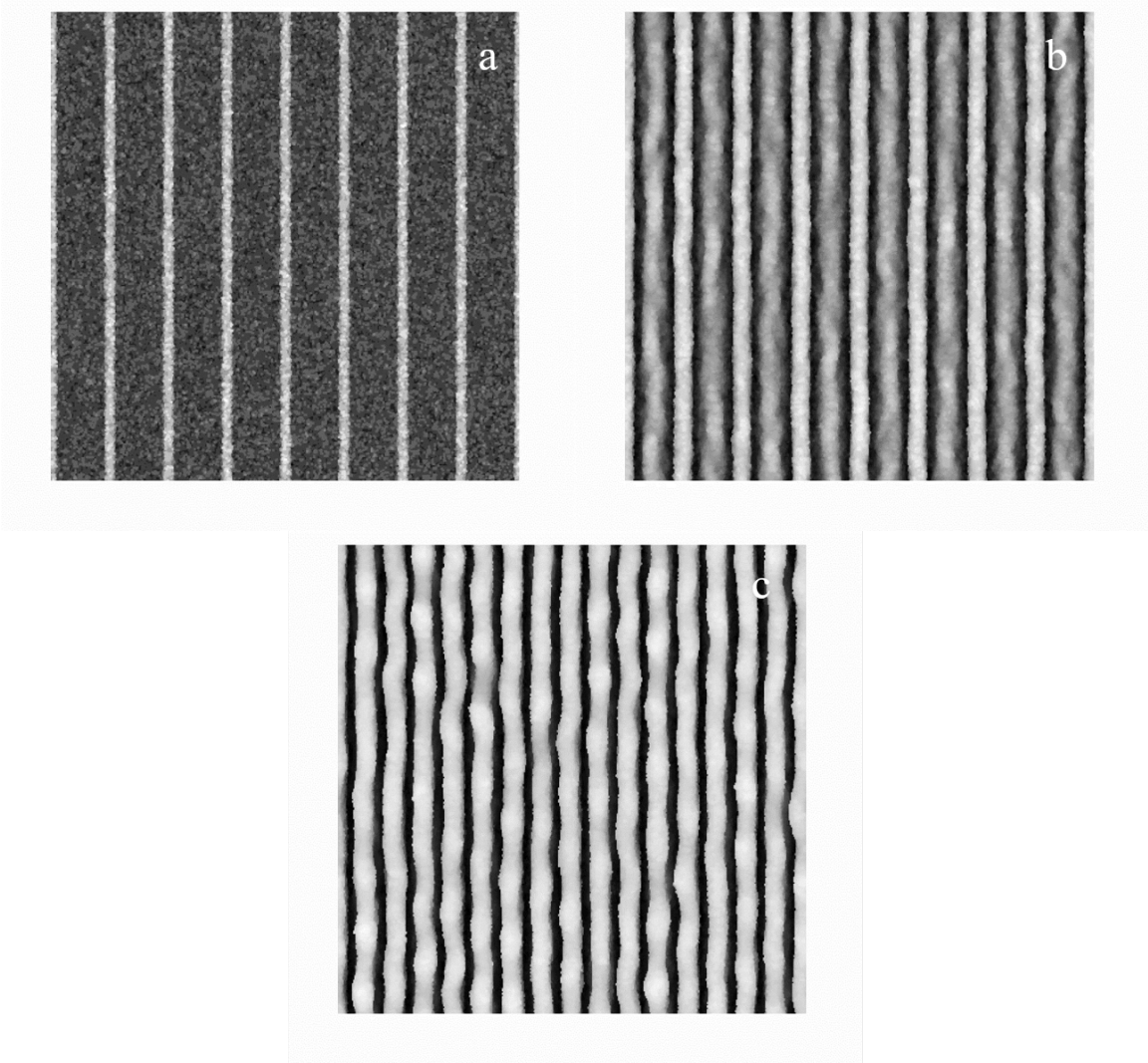

Figure 13: Simulated Film Morphology near 750 nm Pitch Ridges

(a) Initial simulation iteration showing only the ridges and random nucleation. (b) Intermediate image showing area between ridges growing into early lamellae. (c) Final iteration illustrating the highly straightened growth produced by this substrate.

The next substrate has twice the density of ridges as in the previous simulation. Here there are sixteen ridges with a pitch of 375 nm. The growth in this case is the most straightforward of all the simulations so far. The lamellar growth only occurs at the tops of the ridges. There is not enough space between the ridges to accommodate the development of lamella on the substrate surface. Growth is straight for all the lamella, because they are all constrained to grow on top of the ridges. As noted before, the ultimate lamellar pitch differs from the planar case. Here the lamellar pitch matches the pitch seen in the previous simulation, with 375 nm between lamellae.

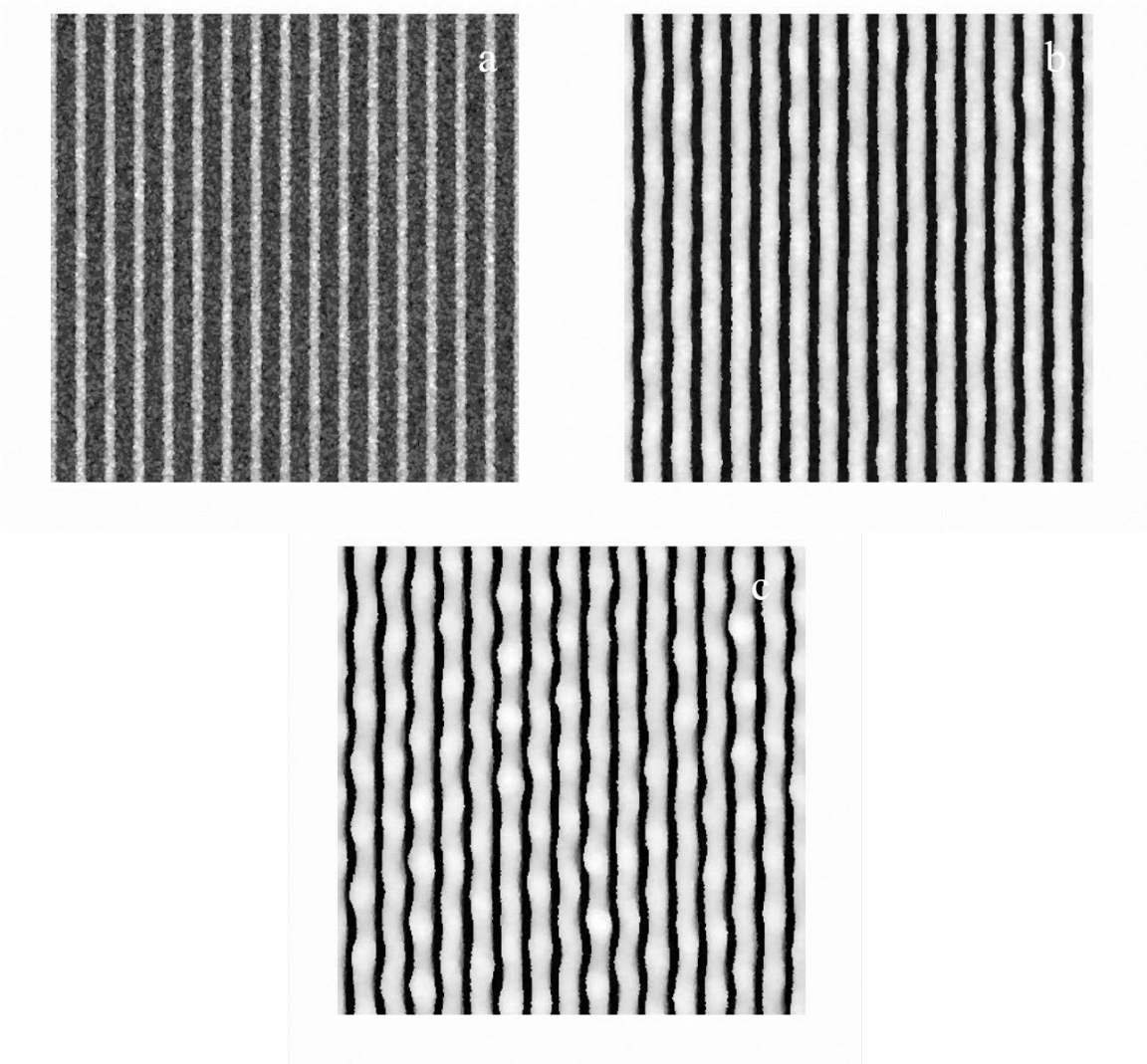

Figure 14: Simulated Film Morphology near 375 nm Pitch Ridges

(a) Initial simulation iteration showing the many ridges on the substrate. (b) Intermediate image with lamellae growing directly up from ridges. (c) Final iteration depicting straight growth.

The final simulation in this set has double the ridge density of the previous example. The thirty two ridges are spaced with a pitch of 187.5 nm. Initially the growth takes place on top of all the ridges to an equal extent. This growth is unstable, however. Due to the small spacing between the ridges, the scattering from a ridge supports the growth on ridges one ridge removed from it. The scattering of light does not reinforce growth on the nearest neighbor ridges. It is fruitful to think of the ridges as two interdigitated sets of ridges, each of which scatters light preferentially among its members. Eventually, once enough material has been added, one set of ridges will randomly have more mass than the other, and the scattering from that set comes to dominate the overall light scattering that takes place. This results in greater light absorption in one of the two sets of ridges, which in turn results in faster growth on that set. This process feeds back on itself, with the ridge set that absorbs light better growing faster, which in turn makes that ridge set absorb light even better still. In the simulation, one set of ridges begins overtaking the other across the entire substrate at once. This indicates that this process is cooperative and somewhat long-ranged. How long-ranged this ordering effect is could not be determined from the simulations, as the computer used for the simulations had difficulty handling larger simulation volumes. What would happen at the interface between regions where different sets of ridges predominated remains an interesting, unanswered question. In this simulation, as before, the final pitch of the lamella is not the expected pitch. However, the pitch of the original ridges was apparently too small for the lamella to accommodate. The pitch ended up converging to that seen in the previous two simulations.

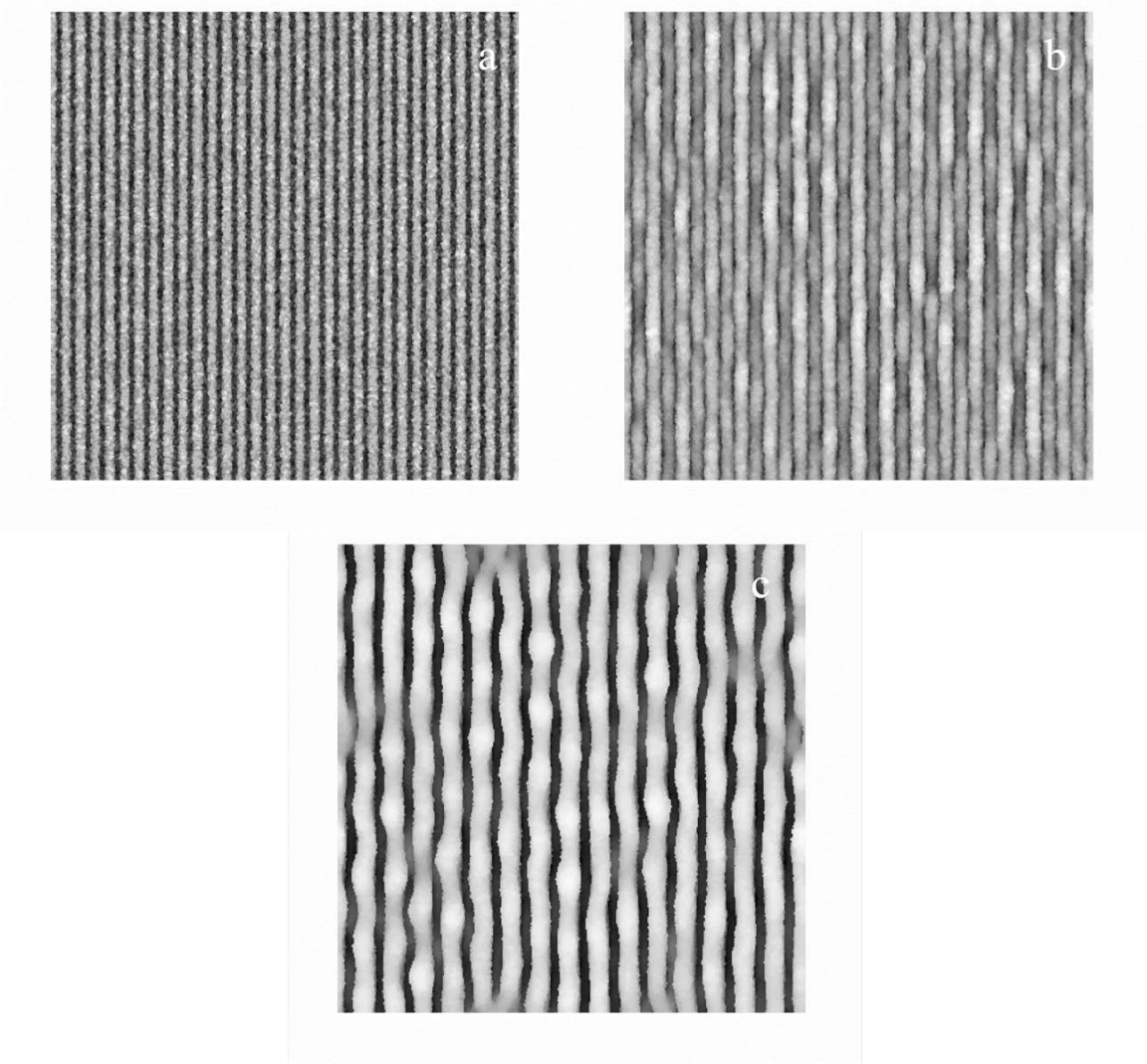

Figure 15: Simulated Film Morphology near 187.5 nm Pitch Ridges

(a) Initial simulation iteration showing many closely spaced substrate ridges. (b) Intermediate image where one set of ridges begins to predominate. (c) Final iteration with the structure converged to that in previous simulations.

3.5 Lithographically patterned substrates

To validate the predictions made by the simulation with an elevated strip on the substrate, silicon substrates were prepared to match the simulated substrate geometry. Non-photoactive, degenerately doped (100) wafers (Addison Wafers, p type, B doped, $\rho < 0.005$ Ω·cm) were cleaved into 15 mm strips and cleaned with deionized water, acetone, isopropanol, acetone, and then water before being etched for 30 seconds in buffered hydrofluoric acid (Transene). Wafer pieces were then transferred to a quartz tube and placed in a tube furnace (Carbolite). The tube was purged with a flow of 2 standard liters per minute of argon. The tube was then heated to 1000° C. The argon flow was then bubbled through deionized water held at 95° C to incorporate water vapor into the argon stream. The wet thermal oxidation of the wafer was allowed to continue for 1 hour, at which time the argon was rerouted so that it was no longer carried water vapor into the tube. The furnace heater was turned off, and the sample was allowed to cool to room temperature.

The thermal oxide was then prepared for photolithography. The SiO_2 surfaces were cleaved into approximately square pieces before being washed with water, isopropanol, acetone, isopropanol, and water sequentially. They were then loaded into a spin coater (Laurel Technologies Corporation) and treated with MCC Primer 80/20 (Microchem). The surface was coated with the primer by spinning it at 3000 rpm for 1 minute, after which time the sample was placed on a hotplate held at 125° C for 1 minute. The wafer pieces were placed back into the spin coater, and the surface was covered with S1813 photoresist (Microchem). The resist was spun to a uniform thickness at 3000 rpm for 1 minute. The substrate was then soft baked on a 125° hot place for 1 minute. The wafers were then

patterned with parallel lines 3 μm wide. The patterned wafers were developed in MF 319 developing solution (Microchem).

The oxide was removed from the exposed regions by placing the patterned substrates in buffered hydrofluoric acid for 5 minutes before rinsing the substrates with copious amounts of deionized water. The residual photoresist was removed by soaking the wafers in acetone for 10 minutes. The wafers were given a quick 10 second etch to remove any native oxide that had formed on the exposed silicon. They were then placed in a 30% aqueous KOH solution at 30° C for 2 minutes. This etch step removed approximately 200 nm of silicon where there was no SiO_2 to keep the basic solution from etching the wafer. The wafer pieces were removed from the KOH solution and rinsed with water. They were then etched for 5 minutes in buffered hydrofluoric acid to remove the remaining SiO_2 etch mask. The resulting substrates consisted of 4.5 μm flat grooves 200 nm deep into the substrate. The widening of the features was a consequence of the exposure conditions used and undercutting during the first hydrofluoric acid etch of the thermal oxide. Given that simulations predict that the ordering effects that take place at the surface step edges are relatively short-ranged, the exact width of the grooves is believed to be of little importance.

Wafers were then scribed into roughly 5 mm by 5 mm squares. Ohmic contacts were made to the backs of the electrodes using a eutectic mixture of gallium and indium scratched in with a tungsten carbide scribe. Electrodes were mounted to an aluminum rod using flash dry silver paint. Nitrocellulose-based nail polish was used to seal the edges of the electrode and to cover any exposed metal. Electrodes were etched for 10 seconds in buffered hydrofluoric acid immediately before being used.

Photoelectrodeposition was performed potentiostatically at -0.2 V vs Ag/AgCl (CH Instruments, 1 M KCl solution) for either 75.0 seconds or 150.0 seconds using a Bio-Logic VMP-3 multichannel potentiostat. The plating bath was an aqueous solution composed of 20.0 mM SeO_2 (Alfa Aesar, 99.5%), 10.0 mM TeO_2 (Sigma Aldrich, 99%) and 2.00 M H_2SO_4 (J. T. Baker. ACS Reagent Grade). A 6 mm diameter graphite rod (Sigma Aldrich, 99.995%) was used as the counter electrode. Samples were illuminated with a broad spectrum halogen lamp fitted with an ELH bulb. The light was directed through a glass diffuser (Thorlabs, DG20-600) before being passed through a wire grid polarizer (Edmund Optics, #34-254) into the electrochemical cell. A photodiode (Thorlabs, FDS100) inserted into the electrochemical cell was used to measure light intensity. The intensity was tuned to 25 $mW \cdot cm^{-2}$ by adjusting the positions of the lamp and the polarizer. The grooves in the substrate were aligned to the edge of the electrode body to which the substrates were attached, and the polarizer was aligned so that the polarization direction lined up with the long dimension of the grooves.

SEMs of the resulting morphology match well with the simulated structure near the step edge. In the short, 75 second depositions, the lamella immediately adjacent to the ridges are much more pronounced than the lamella in the planar portion of the electrode. This is the result of light being most strongly scattered to the areas immediately adjacent to the ridges. The anisotropic scattering that directs light preferentially to the lamella immediately adjacent to the ridge causes those lamella to grow more rapidly that the lamella elsewhere on the electrode. This explains the contrast between these lamella and the other lamellae on the surface.

After 150 seconds of growth, the rest of the surface appears to have effectively caught up with the lamellae immediately adjacent to the surface discontinuity. The increased resistance of the longer lamellae would reduce the amount of current that flows to the tip of those lamellar relative to the current through the shorter lamellae. The straightened lamellae match the straightness of the lithographically patterned feature. These straight lamella continue unbroken for upwards of 100 μm. They are also well localized to the substrate structure that generates the pattern. Examination of the SEMs shows that the disorder of the lamellae far from the step edge is similar for lamellae further from the step edge than nearest neighbor lamellae. This observation matches well with the simulated prediction.

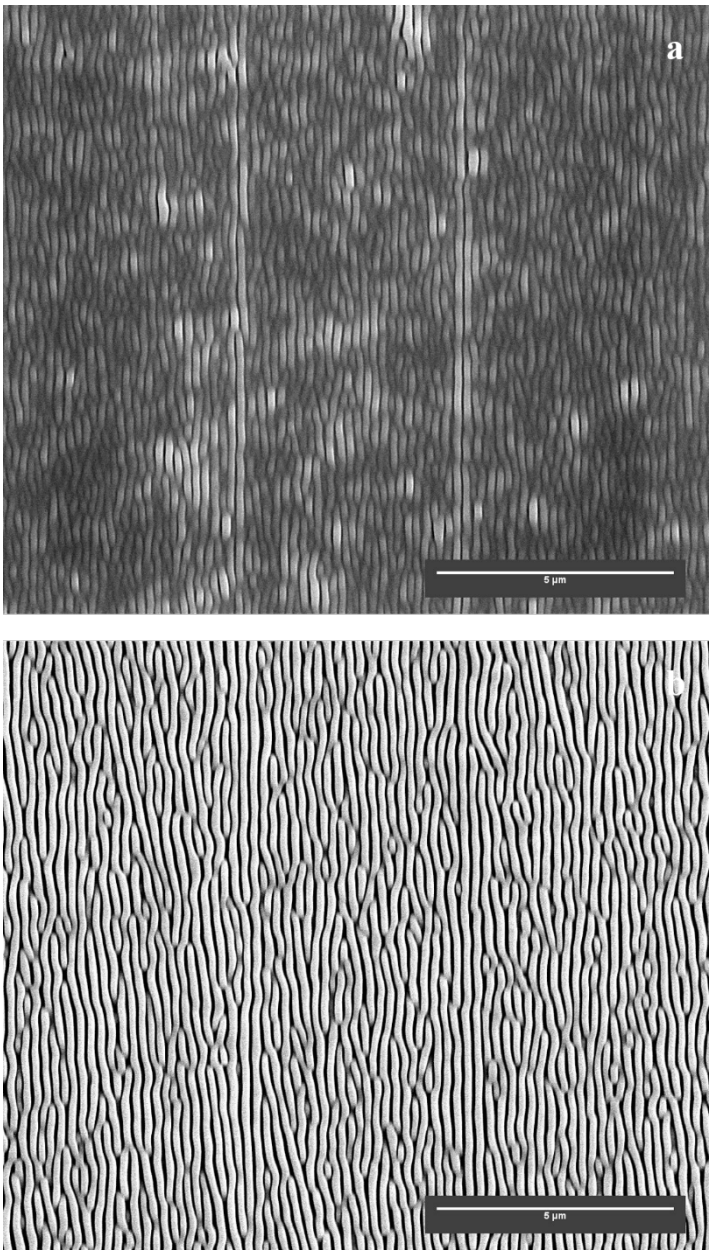

Figure 16: Lamellar Structure at Lithographically Defined Step Edges

(a) Early stage lamellar growth (75 seconds elapsed). (b) Final structure after 150 seconds of growth.

The ordering effect of the step edges is promising, but the short range of the effect limits the ability to get extremely high fidelity periodic patterning of long areas. In an attempt to find conditions that result in regular patterns over larger areas, shorter wavelength illumination was investigated. Previous reports on these self-ordering films have shown that at short wavelengths, nodules form along the length of the lamella. These nodules are believed to be the result of a nearfield optical scattering effect. The short range of this light scattering results in nodules ordered more regularly than the lamellae themselves. The aim in using short wavelengths for depositions in this case was to determine if the highly ordered growths that develop near the substrate features are able to enforce order out to greater distances than in the long wavelength case.

Lithographically patterned electrodes were fabricated as previously described. Control electrodes were made of 5 mm by 5 mm square pieces of a wafer from the same cassette as the wafer that was lithographically patterned. The control electrodes were contacted with GaIn eutectic and sealed to the electrode bodies with flash dry silver paint. The electrodes were sealed with nail polish, and electrodes were etched immediately before use. The electrodeposition was conducted using the same conditions as those used for the electrodes illuminated with the broadband light source, except that the samples were only deposited for 150.0 seconds. The light source used was a 420 nm light emitting diode (Thorlabs, M405L3) collimated into a beam. The optical setup was the same as the one used in the previous experiment, except that the polarizer was rotated so that the polarization direction was normal to the groove direction so that the step edge would have an ordering

effect on the secondary nodule growths. The power output of the LED was adjusted such that the intensity at the electrode was 20 $mW \cdot cm^{-2}$ as measured by a photodiode.

The SEM of the control electrodes shows ordered nodules throughout the surface. These growths pack closely together, and they are grouped into snaking chains that undulate substantially. The secondary growths are much better ordered in the SEM taken of the structured electrode. The top half of the image is the portion of the silicon wafer that was protected from the KOH etch by the SiO_2 etch mask, while the bottom half is the groove produced by the etch process. The nodules at the step edge are very well ordered on both sides of the step. On the upper surface, the ordering of the nodules persists for three rows away from the edge, verifying that the substrate induced ordering of these growths is stronger than for the longer wavelength lamellar growths. On the lower, etched surface, the fidelity of the pattern remains excellent up to several microns away from the surface step. This shows that, using a structured substrate, it is possible to translate a feature size accessible by simple, laboratory photolithography (~μm) into sub-wavelength features using a low cost photoelectrochemical treatment.

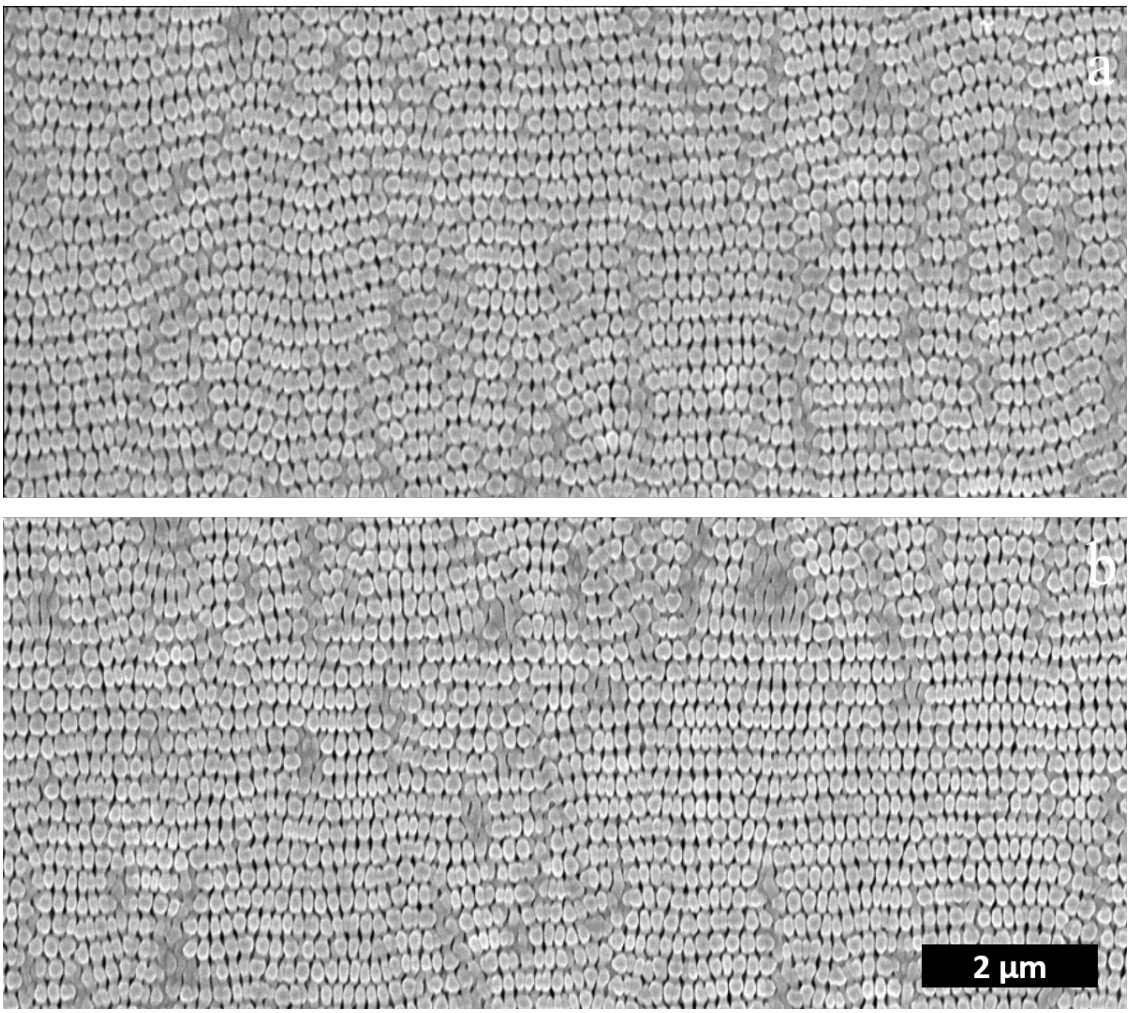

Figure 17: Secondary Lamellar Structure at Lithographically Defined Step Edges

(a) Control electrode with undulating nodular growth. (b) Structured electrode with large patches of well oriented nodular growth.

3.6 Abraded Substrates

The ability to deposit high fidelity structures in registry with defined features on the electrode surface increases the feasibility of using photoelectrodeposition of lamellar films to complement traditional higher precision patterning techniques. However, the greatest control of the growth morphology of these selenium tellurium films was achieved when the surface texturing size was commensurate with the final feature size of the resultant films. The best simulated film fidelity was observed when the ridges were spaced approximately one lamellar period apart. However, if it is possible to generate that ridge pattern lithographically, then the growth of lamellae on top of that pattern provides negligible benefit. If one wishes to leverage the self-structuring of the lamellar films to pattern structured surfaces, the treatment required to structure the underlying substrate should ideally be low cost.

This observation motivates the return to studying the abrasions that were believed to be the origin of the original observations of highly oriented domains. The abrasions on the original films were all adventitious and in general there were abrasions running in many different directions. Intentional abrasion of the electrode surfaces would produce a more uniform distribution of microscopic surface scratches, both in terms of the orientation of the scratches and in terms of their distribution across the electrode surface.

To abrade electrode surfaces uniformly, a cubic block of aluminum measuring 5 cm on a side was placed on a hot plate heated to 150° C. Several flakes of QuickStick 135 mounting wax (EMS Diasum) were added to the top of the heated block. Once the wax had

melted, it was spread uniformly over the surface of the block. A 5 cm square piece of silicon was pressed into the adhesive, and the block was moved off the hot plate to cool. A slurry of 1 μm diamond particles (Micro-Di) was added to a 30 cm diameter polishing pad. An aluminum rail was clamped in place on the pad, and the block with the wafer mounted to it was held against the rail with the wafer in contact with the slurry. The block was then repeatedly moved across the surface, using the rail to ensure that all the abrasion took place in the same direction. The wafer was moved approximately 20 cm across the polishing pad 100 times to ensure the entire wafer would be abraded. The wafer and block were then rinsed with deionized water and heated to 150° C to melt the mounting wax. The wafer was then removed and allowed to cool to room temperature. It was then washed with soap, water, isopropanol, acetone, isopropanol, and water sequentially. The resulting electrodes featured parallel abrasions across their entire surface.

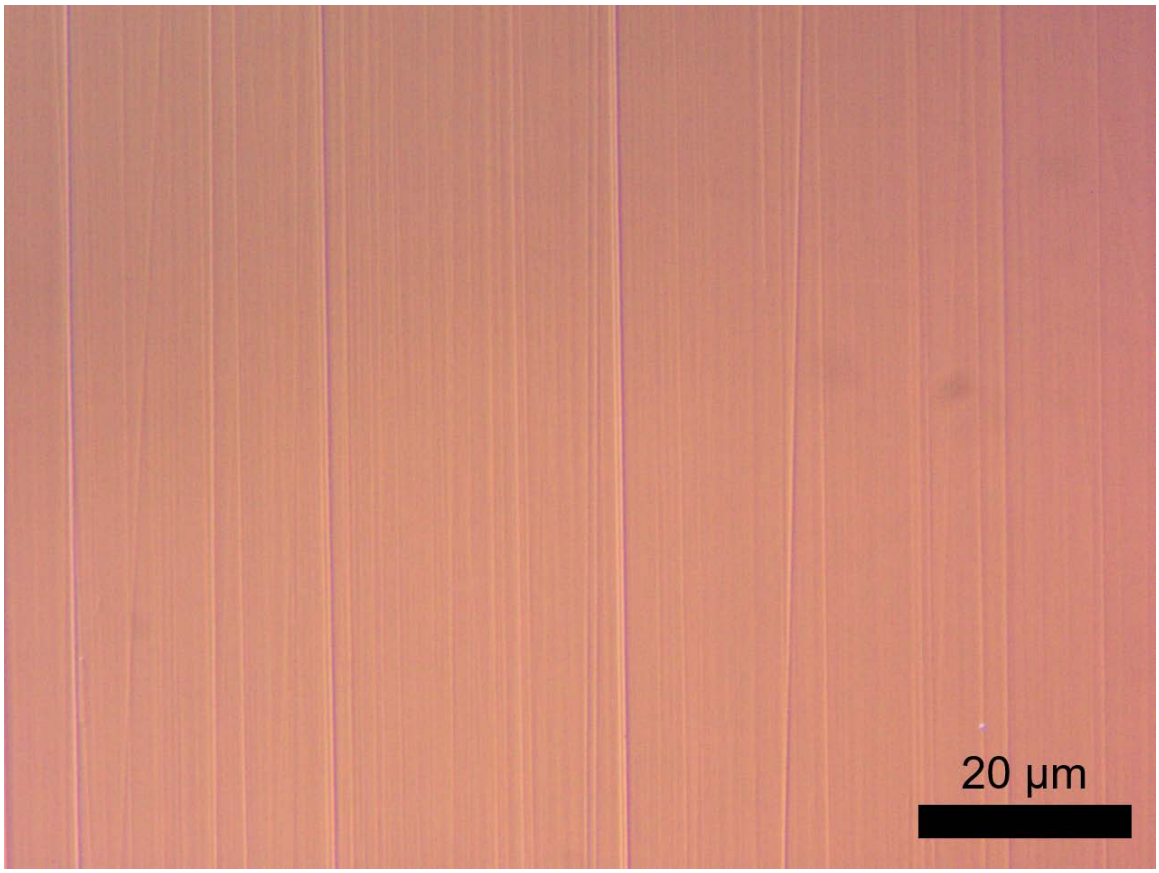

Figure 18: DIC Image of Abraded Surface

Differential interference microscope image of an abraded silicon sample. Scratches of many different sizes cover the silicon surface.

Lamellae were grown on the abraded substrates using both highly monochromatic, 532 nm laser light and broad band light from an ELH halogen lamp. All electrodes were fabricated as previously described, as were control electrodes. In both cases the illumination power incident of the electrodes was tuned to 25 $mW \cdot cm^{-2}$. The polarization direction of the light was set to be parallel to the scratch direction.

The SEMs taken of the electrodes illuminated with the 532 nm laser during deposition reveal the striking effect of substrate texturing on the resultant film morphology. The control SEM shows the sort of growth expected; the deposit is certainly ordered, but the lamellae tend to curve at random, producing a sinuous network of material. The Fourier transform of the control image shows this relative disorder. Most of the intensity in the transform is in the broad spots on either side of the image center. This indicates that the periodicity that we would assign to the lamellae is not truly regular. There must be many different inter-lamellar distances to produce all the frequency components seen in the Fourier transform. It can also be seen from the transform that the lamellae grow at a wide range of angles. The intensity at points off of the main axis of the transform reflects the presence of spatial frequency components that are not perfectly normal to the polarization direction. If all the growth were well aligned, there would not be the vertical spread in the bright spots. The tightly spaced frequency components above and below the center of the Fourier transform represent the nodules that form along the length of lamellae. These nodules are more consistently spaced, as can be seen by the narrowness of the spot. However, owing to the wavering of the underlying lamellae, what would ideally be a small spot has been stretched into an arc.

The SEM from the abraded electrode differs substantially from the SEM of the control. The lamellae are clearly much straighter, even by eye. There is also much less void space between the lamellae. Single lamellae are seen to travel in a straight, unbroken line across the entire image. Compare this behavior to that seen in the control sample, where a single lamella will typically only persist for several microns before being subsumed by another lamella. There is a much greater abundance of nodules along the lamellae for the scratched substrates. Because the nodules grow through nearfield, highly directional scattering, it is plausible that curved lamellae are less able to support these secondary structures. Nodules can only grow on top of existing lamellae, so if there is a kink in a lamella, the near field scattering near that kink would potentially end up in open space where it would be incapable of generating a nodule. The Fourier transform of the SEM offers interesting insights, as well. Compared to the Fourier transformed image of the control substrate, most of the horizontal intensity in the transformed abraded image is tightly distributed around the horizontal axis. This means that there is very little intensity from the diagonal spatial frequencies in the transformed image, which is a consequence of the extreme straightness of the lamellae. The vertical spots in the Fourier transform correspond to the periodicity of the nodules growing on the lamellae. The high intensity of those spots reflects the abundance of nodules in the deposit. The intensity of the nodule associated peaks is also more concentrated toward the center of the arc, in contrast to the roughly equal intensity arcs seen from the control sample. The nodules growing on the abraded sample are more consistently aligned than those on the control sample.

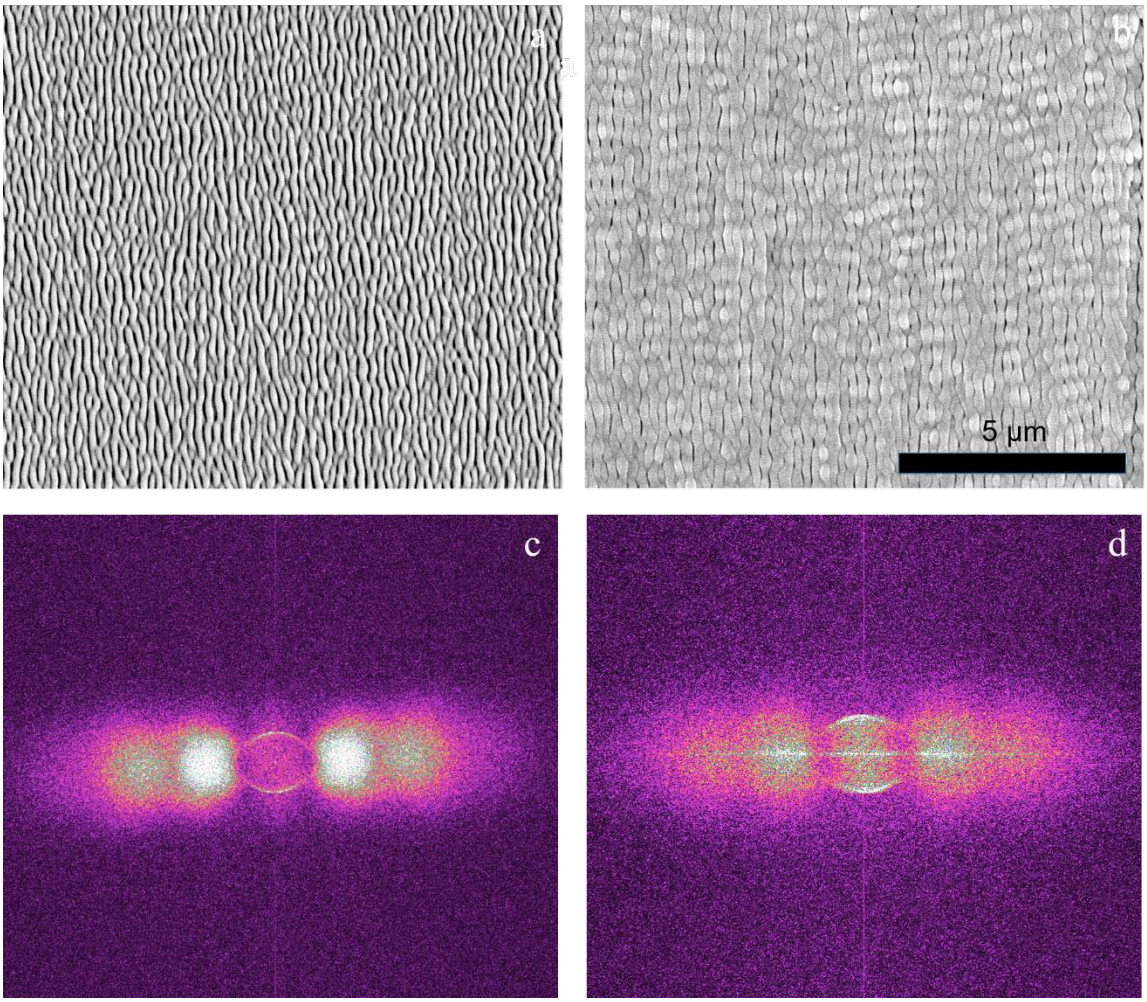

Figure 19: Lamellae Grown with 532 nm Light on Abraded and Planar Surfaces

(a) Control sample grown on a surface without abrasions. (b) Highly straightened lamellae grown on abraded surface. (c) FFT of panel a. (d) FFT of panel b.

The morphology of the white light grown lamellae shared many features with the lamellae grown with laser illumination. In the case of the control sample, the lamellae grow roughly aligned with the polarization direction of the light, but they meander back and forth across the electrode. They often cross paths with other lamellae and either merge with them or terminate into their sides. The average lamella is still relatively short, measuring only a few μm. The Fourier transform of the SEM is similar to that of the green control sample. The transform features large, diffuse spots on the axis normal to the polarization direction. The prevalence of lamellar growth along directions not completely parallel to the polarization axis is clear from the large spots in the transform. There is no vertical spot in the transform, consistent with the fact that the nodules seen in the green sample develop much less readily when the illumination source has more of its intensity coming from red or infrared light.

The abraded sample grown in white light has a dramatically different appearance than the control. The lamellae grow straight across the micrograph, with some small, particulate growth still visible in some places. The lamellae are well separated, with a larger amount of void space visible than in the SEM of the abraded sample illuminated with 532 nm light. While the lamellae are all very straight, the spacing between them varies more than seen in the other samples. This observation is supported by the Fourier transform of the micrograph. The transformed images features a continuous strip of intensity along the horizontal axis. The intensity peaks at the same locations relative to the center of the image as the intensity peaks in the transformed control image. The most common spacing in the abraded sample matches that in the control sample, but all other spacings are represented in the abraded

sample. As before, the Fourier transform confirms the absence of the secondary nodule growth, owing to the long wavelength of the light source.

The wide variation in the spacing between lamellae is a result of the many different scratch widths in the abraded surface. While the abraded sample illuminated by 532 nm light had a single predominant period, that was the result of the light source being a laser, and therefore monochromatic. The halogen lamp light source emits light across the entire visible and near infrared range. Given a diverse range of scattering ridge separations, some ridges will be spaced correctly to optimally scatter specific wavelengths of light, in which case the effect of that wavelength of light will be outsized relative to the amount of the incoming optical power attributable to that wavelength. In the case of white light illumination, the increased spatial ordering from straightening the lamellae comes at the cost of spatial disorder from the widely varying inter-lamellar spacing.

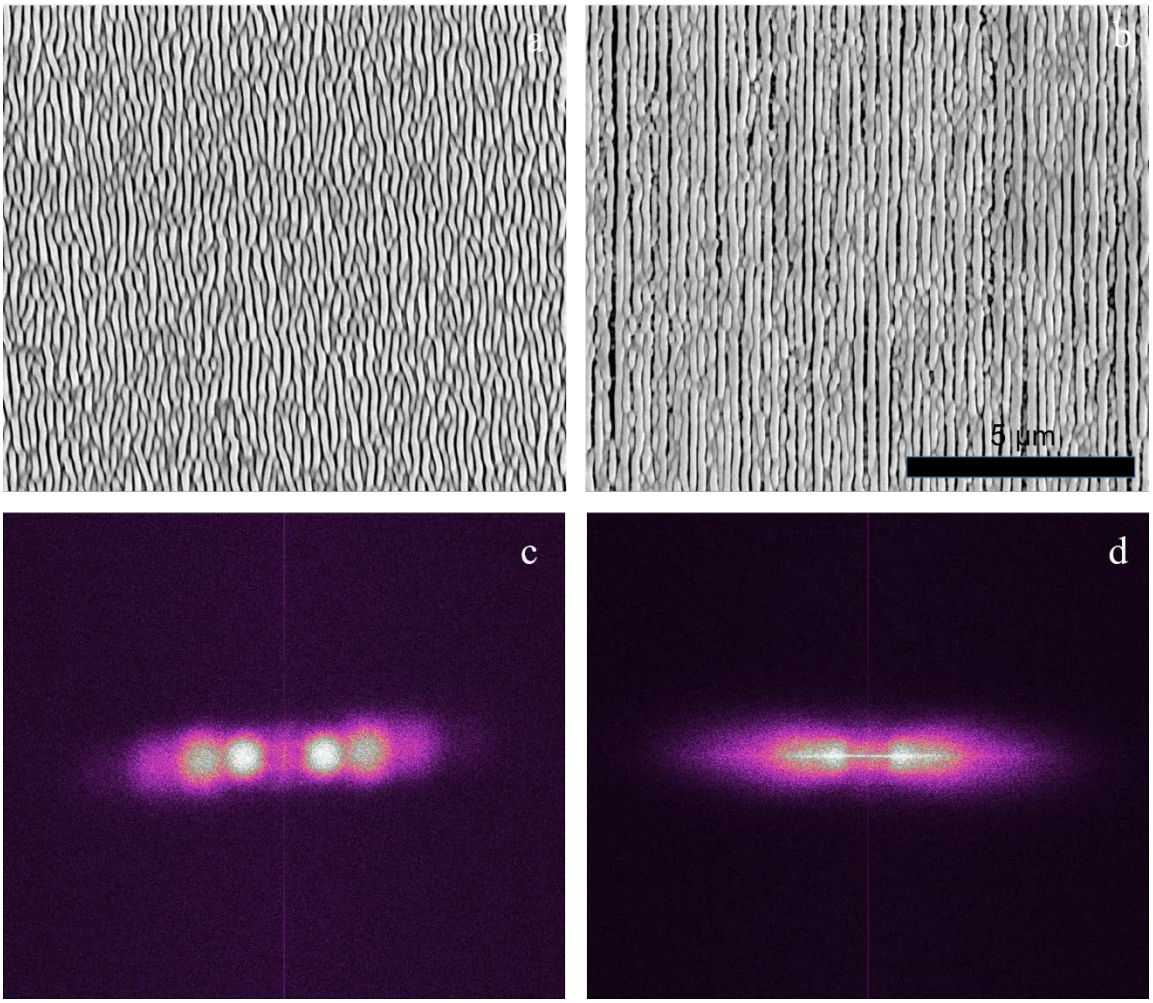

Figure 20: Lamellae Grown with White Light on Abraded and Planar Surfaces

(a) Control sample grown on a surface without abrasions. (b) Highly straightened lamellae grown on abraded surface. (c) FFT of panel a showing round horizontal features. (d) FFT of panel b showing a narrow horizontal line.

3.7 Conclusions

Understanding the role that substrate structuring plays in influencing the morphology of photoelectrochemically deposited lamellar structures expands on the toolset available to generate bespoke nanostructures *via* simple, solution phase processes. The use of patterned electrodes has been shown to be an effective, low cost way to improve the pattern fidelity. The use of varied surface features joins the use of different optical inputs to dictate film morphology.

While this particular study is complete, it suggests many potential fruitful avenues for future researchers to pursue. There is an interesting interplay between the periodicity of the substrate and the wavelength of the light source, as evidenced by simulations and the morphology of the structures grown on abraded surfaces under white light illumination. However, the relationship between the two factors is not fully understood. Furthermore, as will be discussed in the following chapter, there is value into getting an extremely periodic lamellar pattern across macroscopic areas for the purposed of optical device fabrication. The result that the nodules pattern very nicely near step edges is a promising first step. What remains to be done is to optimize the deposition conditions and grow these structures on substrates with smaller, roughly 1 μm separations between the step edges. Finally, this study illustrates that lamellae deposit adjacent to the step edges. A quantitative investigation of this behavior would be of interest in the context of multiple patterning.

Chapter 4

STRUCTURAL COLORATION OF SELF-STRUCTURED PHOTOELECTRODEPOSITED SEMICONDUCTING FILMS

4.1 Introduction

Though most familiar coloration comes from pigments and their absorption of specific wavelengths of light, there are many other examples of color arising from the microscopic structure of a material.[62–65] The iridescent color of soap bubbles is a consequence of interference taking place in the thin soap layer at the edge of the bubble.[66] The colorful, angle dependence appearance of CDs, DVDs, and the holograms on credit cards is the result of diffraction off of microscopic surface features. Structural color is also the source for many of the most striking colors found in nature. The blue coloring in peacock feathers and *Morpho* butterfly wings is the result of microscopically structured material that preferentially reflects specific wavelengths.

The development and characterization of microscopic structures that interact with light in an angle dependent, polarization dependent, and wavelength dependent manner has generated substantial scientific interest.[67–71] Because the color of these structures depends crucially on their microscopic geometry, researchers have many degrees of freedom with which to manipulate the optical response of these materials. Both alterations to the structure's overall geometry and the specific dimensions of the structure can have dramatic effects on the color of the material. Many different fabrication techniques have been brought to bear on

the problem of how to create these structures. High capital cost processes such as photolithography and e-beam lithography have both found substantial use in patterning surfaces to create grating-like structures.[72,73] Colloidal self-assembly of nanoparticle templates has been used to make three dimensional photonic crystals, though only a limited class of structures are accessible by using this technique.[74–76] Two-photon lithography has been used to create many diverse structures that extend out of the plane of the substrate, though the process is both expensive and serialized.[77,78]

The photoelectrodeposited films discussed in the previous section spontaneously develop subwavelength features spaced regularly across the electrode surface. These periodic structures are similar to those found in devices designed to exhibit structural color. In fact, the microscopic structure of iridescent blue butterfly wings is very similar to the structure that the selenium tellurium films discussed in the previous chapter naturally adopt. The morphology of these structures can also be modified using the host of techniques previously discussed if one wished to tune the properties of the resulting film. Photoelectrodepositing self-structuring semiconductor films has the potential to deposit structures that exhibit structural color in a low cost, scalable way. The following chapter will consider initial forays into creating structural coloration using phototropic growth of semiconductors.

In considering the potential applications of photoelectrodeposited lamellar structures as optical devices, it is helpful to compare the spontaneously developing film morphology to that of existing structures known for their wavelength and angle dependent light response. Of particular interest are two examples drawn from disparate origins, specifically the structure of holographic diffraction gratings that allows them to separate light wavelength

and the surface structure on *Morpo* butterfly wings that is responsible for the butterflies' deep blue color.

Holographic diffraction gratings are common components used in monochromators and spectrometers to split light into the various wavelength components in the original beam. They are produced by shining two laser beams at a sample coated with photoresist. The two beams interfere and produce a series of intensity fringes across the illuminated surface.[79] This variation in intensity across the surface causes only specific regions of the photoresist to be exposed. When developed, the result is a sinusoidal pattern on the surface of the substrate. These surfaces are given a reflective coating and then used in optical devices. Light incident upon this patterned surface is then diffracted according to the grating equation:[80]

$$n\lambda = d(sin\theta_i - sin\theta_o)$$

Here the spacing between surface ridges is *d*, n is the order of the diffracted light, θ_i is the angle between the angle between the incoming light and a vector normal to the grating surface, and θ_o is the angle between the outgoing light and a vector normal to the surface. In an ideal grating with a constant separation between ridges, only a very narrow band of wavelengths will be measurable at any single outgoing angle.

Butterfly wings also exhibit structure-derived light scattering, though somewhat differently. When viewed under a light microscope, the wings of a butterfly, in this case a *Morpho menelaus* butterfly (ButterfliesAndThings.com), are made up of scales roughly 75 μm long. When viewed in a scanning electron microscope, ridges running along the long axis of the scale become apparent. At further magnification still, one can see that the ridges

have lamellae lining their sides. These lamellae are composed of transparent chitin. The bright blue coloration of *Morpho* butterfly wings is a consequence of a combination of both grating-like diffraction off the lamellae and multi-layer interference through the transparent layers.[81–84] The butterfly wings have a brilliant blue color when viewed from a wide range of angles, though the color does depend somewhat on viewing angle.

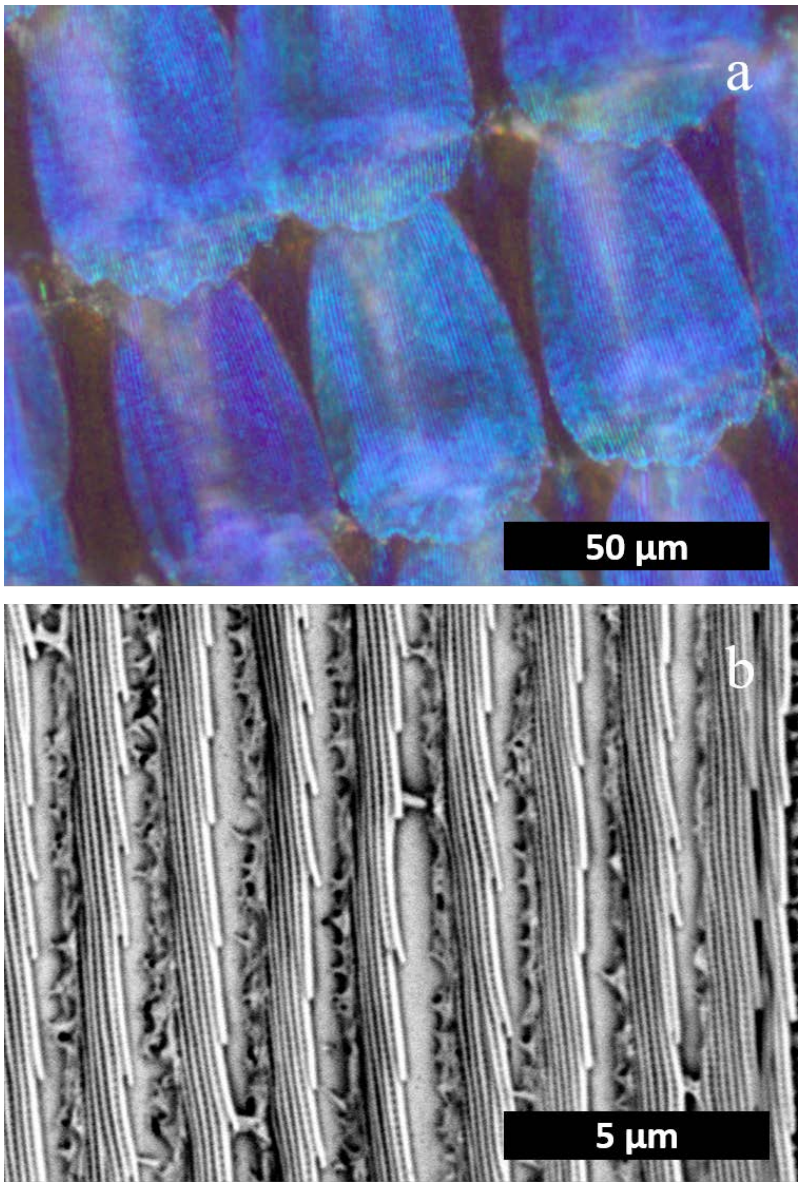

Figure 21: Butterfly wing structure responsible for coloration

(a) Microscope image showing colored scales that comprise *Morpho* wing surface. (b) SEM of the ridges on a scale.

Both diffraction gratings and butterfly wings bear comparison to the lamellar structures discussed in the previous chapter. In all cases, the surfaces are composed of periodic structures. More importantly, like diffraction gratings and butterfly wings, the lamellar structures diffract light in both a wavelength- and angle-dependent manner. For electrodeposited lamellae, this diffraction is most apparent when viewing the electrodes in the plane containing the vector normal to the electrode surface and the polarization axis of the light source used for the deposition. In other words, the coloration is strongest when tilting the sample down the growth direction of the lamellae, rather than tilting the sample such that you are effectively looking across the tops of lamellae. This suggests that there are periodic structures along the length of the lamellae that give rise to the diffraction. Additionally, the brightest samples are those grown under illumination with short wavelength light. The conditions that produce the most iridescent samples also produce the samples with the most prominent nodular growth along the lengths of the lamellae. These facts together suggest that the strong iridescence of these samples is due to the nodules.

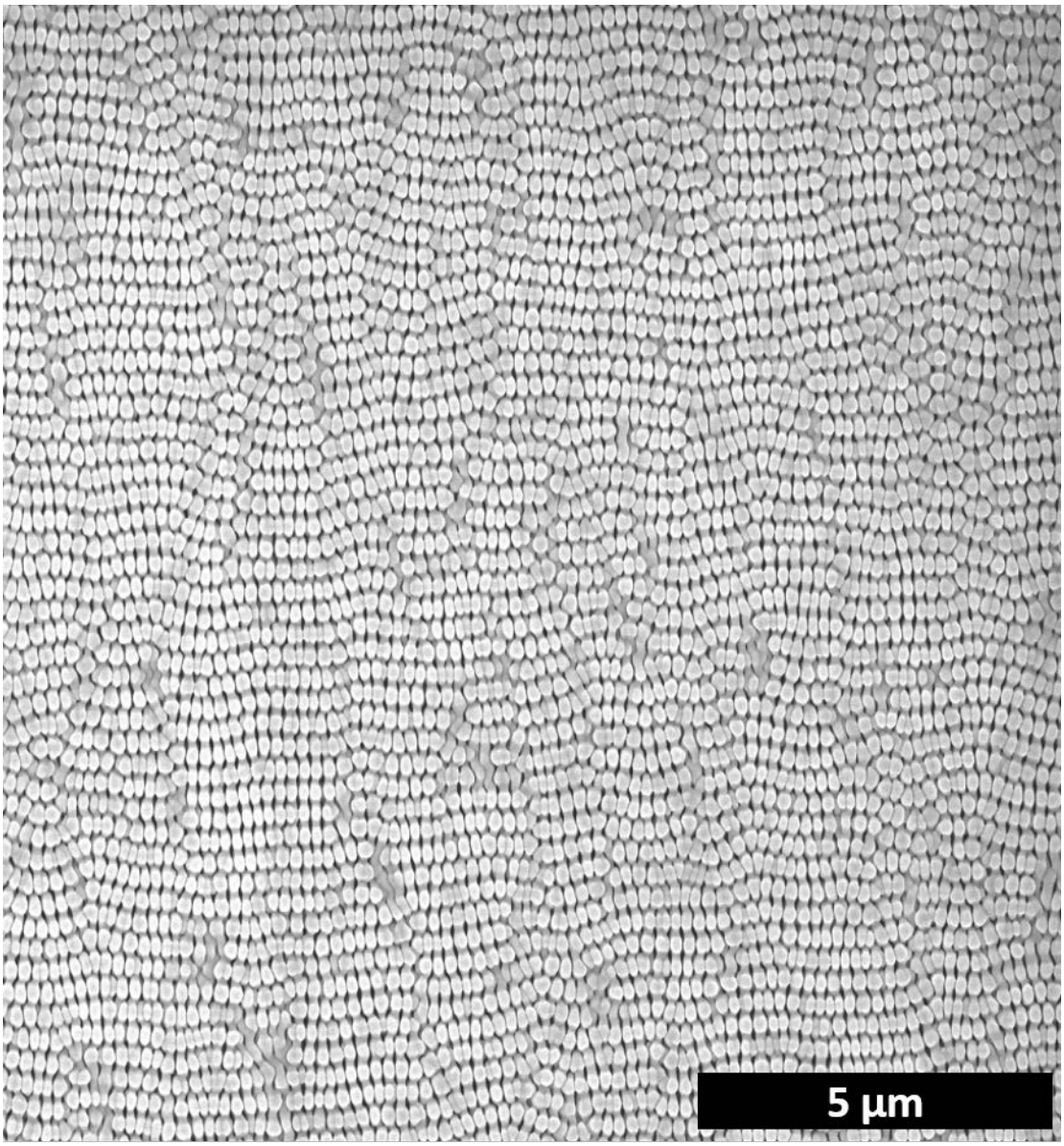

Figure 22: SEM of an Iridescent Lamellar sample

The SEM of this electrode show the surface morphology of a highly colored film. The lamella are hardly visible under the nodular growth. The lamellae are running roughly vertically in this sample.

4.2 Diffraction Characterization

The diffraction from the structured electrode surfaces was characterized by scatterometry. A sample grown under polarized 455 nm LED illumination was analyzed using a VASE Ellipsometer (J. A. Woollam). Scattering spectra were collected with the sample illuminated at incidence angles of 75° and 80°. The detector was moved in 5° increments from 45° from the normal to 10° from the normal. The mechanism of the instrument constrained the detector to move in the plane containing the incident beam and its specular reflection. At each detector position a spectrum was collected from 400 nm to 600 nm at 5 nm increments. The spectra shown illustrate the wavelength selective diffraction from the surface of the structured electrode. At any given instrument, the collected spectra show relatively narrow bandwidth diffracted light, with the peak wavelength dependent on the incident and outgoing angles. The full width half maximum for the spectra is generally approximately 30 nm, indicating that the surface structure as deposited would not serve as effectively in a monochromator as a commercial grating. The relative intensity of the collected light falls off as the detector approaches a position normal to the sample surface. This is in large part a geometrical artifact. At shallower angles, the region of the sample visible to the detector has a larger surface area than the region from which the detector can collect light while nearly normal to the sample. Similarly, the intensity of the spectra is across the board lower when the light source is at a more grazing angle of incidence. At these shallow illumination angles, the spot illuminated by the monochromator is spread across the sample, so that the total intensity incident on the portion of the sample visible to the detector

is lower than at steeper illumination angles, resulting in lower intensity diffracted to the detector.

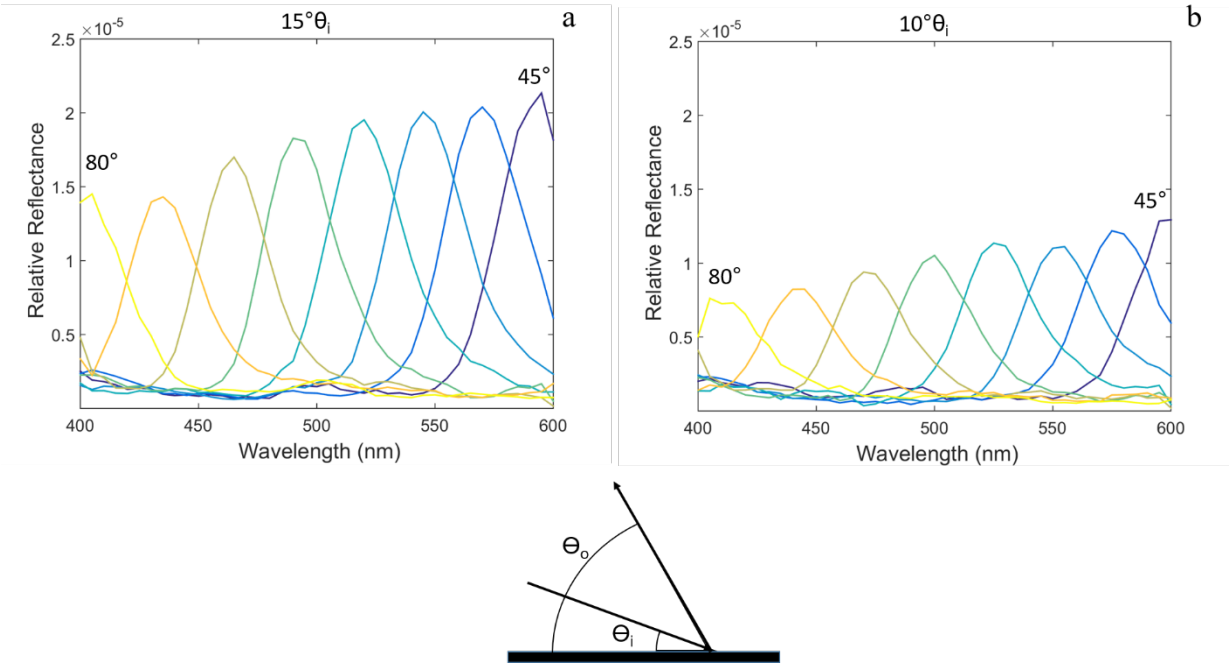

Figure 23: Angle Dependent Diffracted Spectra

(a) UV-Vis spectra collected at 5° intervals of θ_o for θ_i = 10°. θ_i was as defined in the schematic below the image. (b) UV-Vis spectra series collected at θ_i = 10°.

Measurements of diffracted intensity versus detector angle were made at fixed wavelengths. The incident angle was set to 70° and the monochromator was programmed to emit light first at 400 nm and then at 500 nm, and the monochromator width was set to 1950 μm. The detector was swept through the full angular range in 0.5° increments. The aperture on the detector subtends an angle of 0.4°, so using smaller increments for the detector movement would not be productive. The peaks were broad for both wavelengths, with full widths at half maximum of about 5°. The peak positions agree reasonably well with the positions predicted by applying the grating equation, though the peaks are offset from the predicted maxima by a few degrees. The grating equation roughly describes the diffraction from these films, but the fact that it does not perfectly predict the diffraction is not unexpected. The geometry of these samples differs substantially from the idealized geometry of a perfect grating. However, the qualitative agreement with theory confirms that the physical origin of the non-specular light from the surface is from diffraction off of the surface texture.

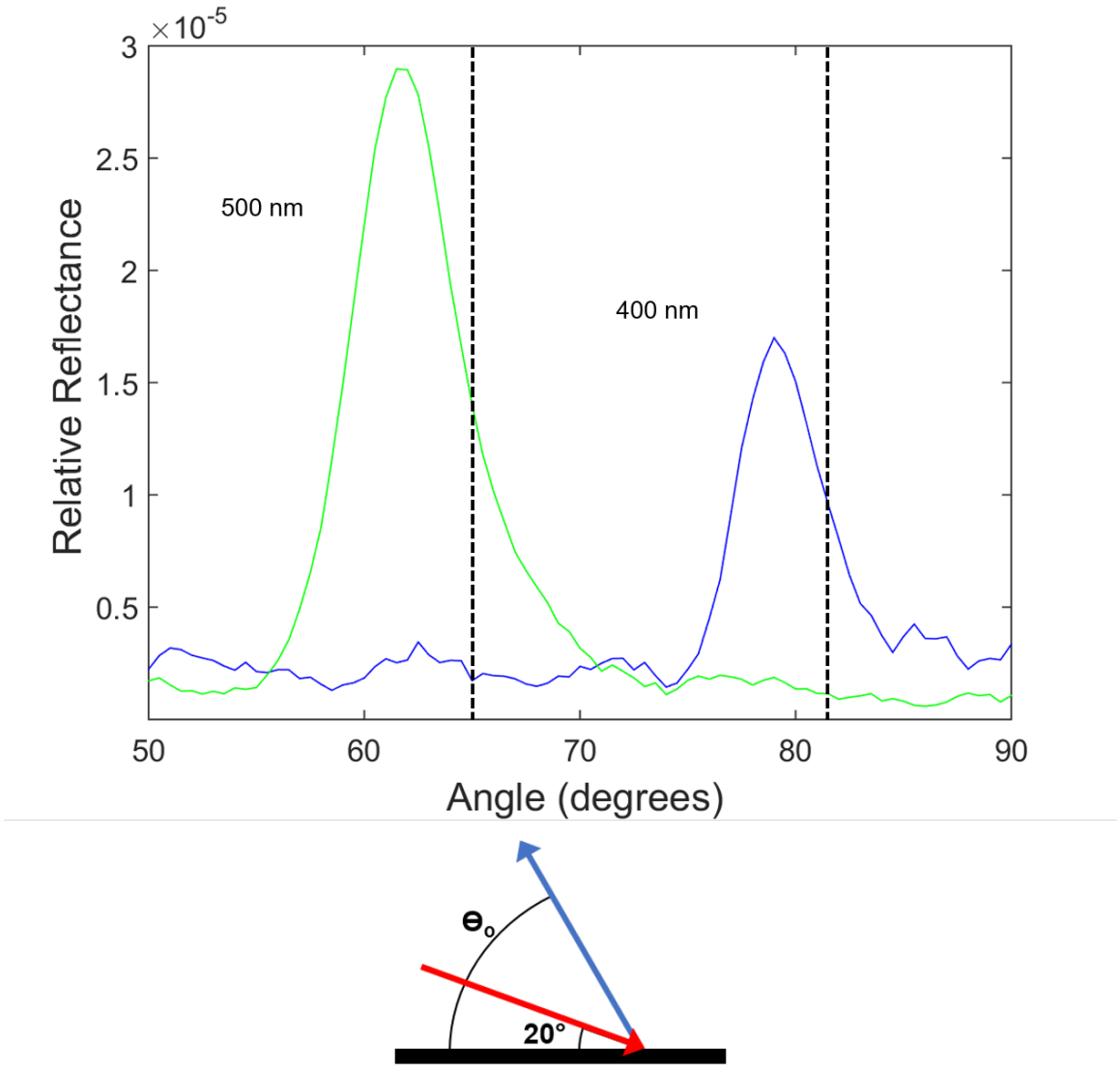

Figure 24: Diffracted light intensity as a function of angle

The light diffracted off the surface, where angles are as measured in the schematic. The predictions from the grating equation are indicated by the black dashed lines. The 500 nm peak occurs at an angle 3.7° shallower than predicted, and the 400 nm peak occurs 3.4° shallower than predicted.

As the material comprising the diffracting surface was a semiconducting alloy of selenium and tellurium, a substantial amount of the incident light was assumed to be absorbed in the material without diffracting. To improve the reflectivity of the surface, a thin aluminum layer was applied to the structured surface. The original sample used in the previous measurements was coated by a 20 nm layer of aluminum *via* RF argon sputtering at 150 W in a chamber with a base pressure $< 5 \times 10^{-6}$ Torr. Subsequent measurements showed that there were substantial increases in light intensity at the detector at all angles and wavelengths. The diffracted intensity was generally roughly fourfold higher off the aluminized sample than off the as-deposited selenium tellurium film. Neither the peak positions nor the line widths changed appreciably following the deposition of the aluminum. This result was expected, as the pitch of the surface structure would be unaffected by the application of a conformal coating. While the spectra collected from the original film had only a single peak, several spectra from the metal coated film featured a second small peak in addition to the main peak. Higher order peaks are expected from diffraction gratings, but they were not observed, either visually or spectroscopically, from the as-deposited samples. The disorder of the electrode surface and the light absorption of the substrate likely reduced the intensity of light in the second order peak below the ellipsometer's detection limit.

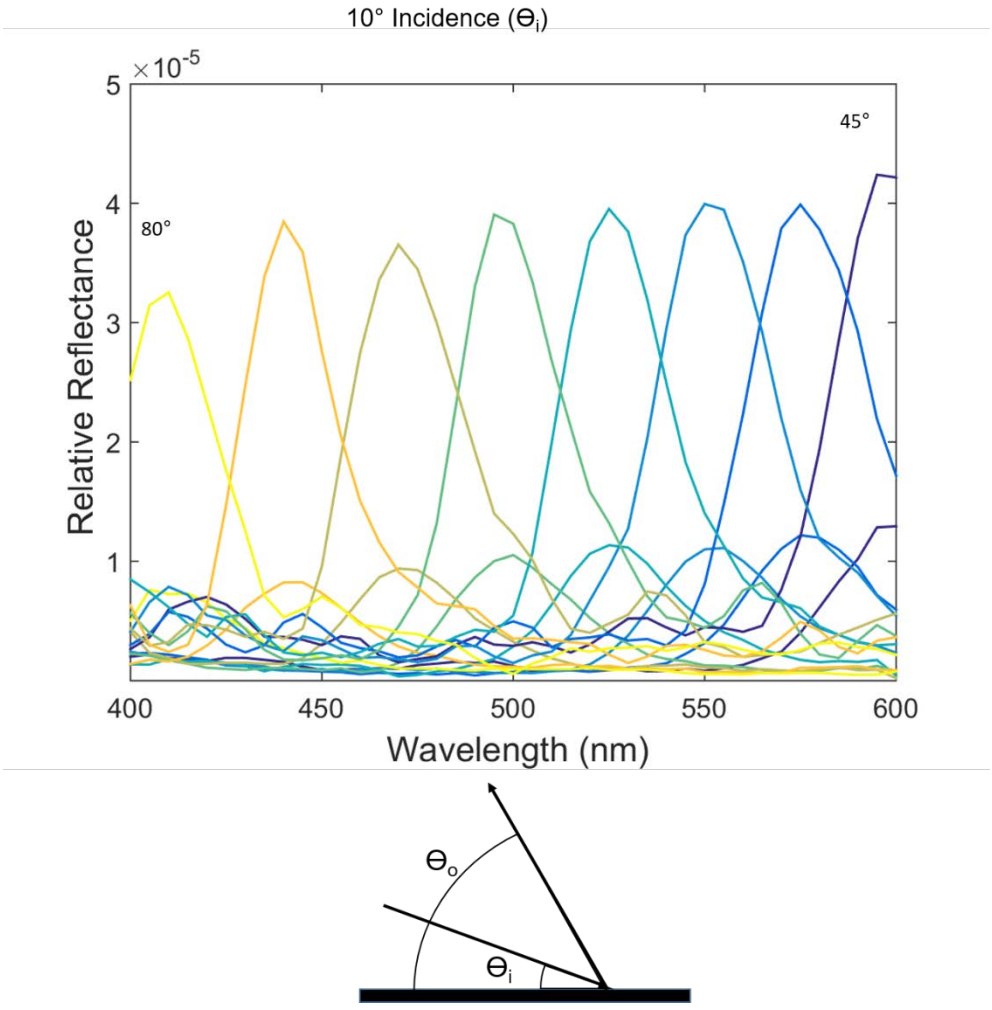

Figure 25: Variable Angle Spectra of As Deposited and Aluminized Films

The upper peaks are the peaks from the aluminum coated sample, while the peaks directly below them are the peaks from the bare selenium tellurium sample. The peaks are identical, except that the aluminized samples are generally four times as bright and some secondary peaks are visible in the aluminized sample spectra.

The detector position in the ellipsometer is constrained to remain in the plane containing the incident beam and the specular reflection. However, a substantial amount of light is diffracted out of that plane by these surfaces. These electrode are strongly colored when viewed from a wide range of angles, much more so than diffraction gratings. Additionally, the fraction of the total intensity diffracted into the detector in the previous measurements is very small, even when the sample had a reflective coating, suggesting that the unaccounted for intensity must be going out of the plane of the detector.

An apparatus to measure the out of plane diffraction was constructed. A screen was placed 30 cm in front of the sample, which was mounted on a rotation stage. A 532 nm laser was directed through a 1 mm aperture and a hole in the screen onto the sample. The sample was rotated, and the light intensity on the screen in front of it was recorded with and Olympus E-PL1 camera. The stationary bright spot is from diffuse light behind the screen passing through the opening in the screen. The bright rectangular spot is from the specular reflection off the surface of the electrode. The electrode was rotated in 5° increments. At higher extents of rotation, a bright band becomes visible on the screen. This is light diffracted from the structured surface of the electrode. Note that the light extends widely out of plane. This explains the low intensity measured in plane. Substantial light intensity extends well over 10° out of plane in both direction. The small spots within the band of diffracted light are the speckle pattern from the laser light.

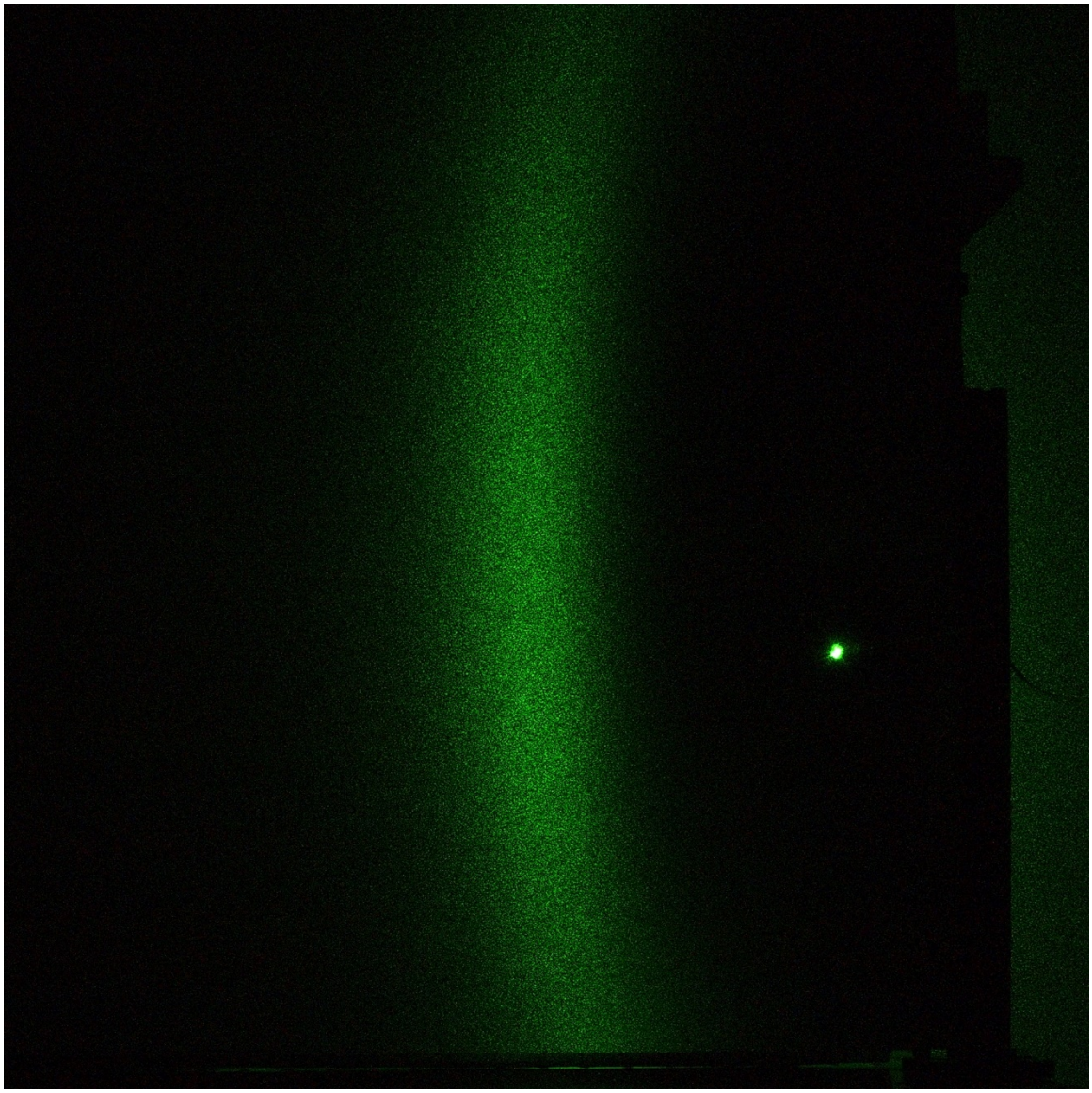

Figure 26: Out of Plane Diffraction Image

532 nm light incident on the sample diffracts into a large area. Here the electrode was rotated 35° counterclockwise of normal incidence, producing a wide band of diffracted light.

4.3 Manipulating Structural Coloration

Since the light diffracted off the surface of these electrodes spreads out into a wide band, it can be concluded that, barring substantial improvement in pattern fidelity, these surfaces are inappropriate for use as gratings. Monochromators require both good resolving power and high efficiency, neither of which these surfaces can provide.

However, the properties of these films that make them unsuitable for use in instrumentation make them more valuable as a source of coloration. Just as the structure of butterfly wings results in broad band diffraction over a wide range of angles, so does the surface morphology of these electrodes. Using these surfaces for coloration is appealing for several reasons. First, the wavelength dependent pitch of the features on the surface means that an arbitrary nodule spacing can be deposited given the appropriate choice of illumination wavelength. This in turn means that the optical response of these surfaces can be easily tuned. Second, the fact that the origin of the color is structural instead of pigment derived means that these surfaces would be immune to bleaching, unlike conventional dyes. Short of being physically destroyed, these films should maintain their color even after exposure to high light intensity, extreme heat, or exposure to chemicals that would destroy pigments. Finally, since these films are more resilient to ionizing radiation than chemical pigments, these films could be used as a source of UV coloration.

The photoelectrodeposition of these films can be conducted successfully at the same potential, regardless of illumination wavelength. Therefore, a single electrode held at a fixed potential can be patterned with different features in different areas by controlling the

wavelength of light incident on different regions of the electrode. Furthermore, it has been demonstrated that the illumination of an electrode with multiple wavelengths of light produces a deposit morphology consistent with illumination from a source with a wavelength intermediate between the two sources used. Using only two light sources, one could potentially pattern an electrode with an arbitrary range of feature spacings in a localized manner simply by adjusting the relative intensity of the sources on a point by point basis.

A consumer home theater projector is well suited to accomplishing the previously outlined tasks. An Epson Home Cinema 2150 LCD projector was chosen as the light source for the following depositions. Two 50 mm focal length biconvex lenses were mounted on a rail in front of the projector and were adjusted to bring the projector image in focus 15 cm from the projector. An electrochemical cell was placed such that light from the projector would focus on the surface of an electrode in the cell, and a wired grid polarizer was mounted in the path of the beam. A fiber coupled UV-Vis CCD spectrometer was used to collect spectra from pure red, green and blue images. These images were full screen projections of a single defined color, with (255,0,0), (0,255,0), and (0,0,255) being the decimal code RGB values of red, green, and blue respectively. The spectra revealed that multiple light sources contribute to the red, green, and blue pixels. A FDS100 photodiode was used to measure the photocurrent density for each color. The photocurrent densities of the pure colors were 12.9 $mA \cdot cm^2$ for red, 18.5 $mA \cdot cm^2$ for green, and 9.0 $mA \cdot cm^2$ for blue.

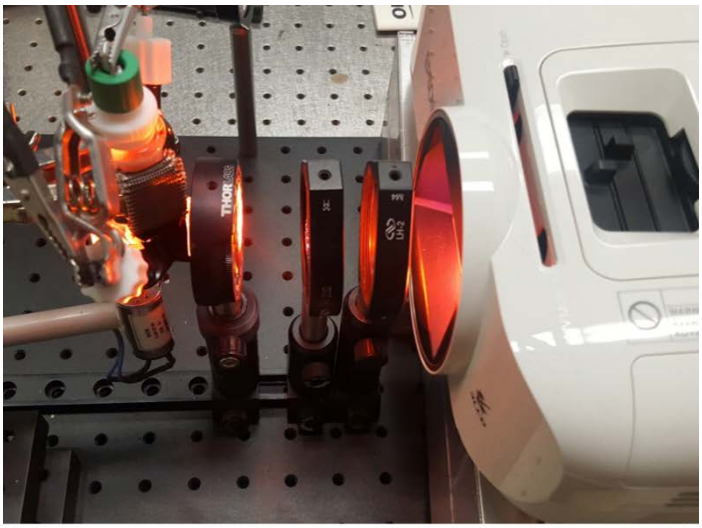

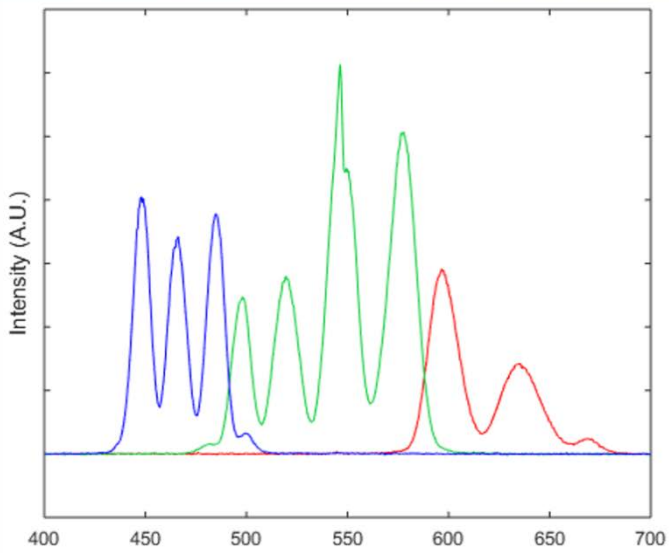

Figure 27: Projector Illuminated Depositions

The projector was configured to illuminate electrodes as shown. The UV-Vis spectra of purely blue, green, and red images showed multiple peaks for each color.

Electrodes used in the following depositions were fabricated in a similar manner to those previously described. Single side polished (100) silicon wafers (Addison Semiconductor, n type, P doped, $\rho < 0.005\ \Omega\cdot$cm) were etched in buffered hydrofluoric acid (Transene) and loaded into a metal evaporator at a base pressure < 10^{-5} Torr. A 10 nm adhesion and ohmic contact layer of titanium (Kurt J. Lesker Company, 99.995%) was deposited *via* electron beam evaporation at 10 kV accelerating voltage and 40 mA emission current. A 50 nm gold layer (Kurt J. Lesker Company, 99.999%) was subsequently deposited at 10 kV accelerating voltage and 140 mA current. The wafers were then flipped and an ohmic back contact of 100 nm of titanium was then deposited at the same conditions as on the polished side. Wafers were scribed into 1 cm by 1 cm squares and mounted to electrode bodies with flash dry silver paint (SPI Supplies). Nitrocellulose based nail polish was used to seal the sides of the electrode and block any exposed metal on the electrode support. Gold was chosen because concurrent research in the group had shown that higher quality lamellar patterns form on noble metal surfaces than on lower work function materials. Gold was selected as the surface material over platinum because it allowed the use of more negative potentials during deposition without competitively producing hydrogen.

Photoelectrochemistry was performed potentiostatically at -0.2 V vs Ag/AgCl (CH Instruments, 1 M KCl solution) for 600.0 seconds using a Bio-Logic VMP-3 multichannel potentiostat. The plating bath was an aqueous solution composed of 20.0 mM SeO_2 (Alfa Aesar, 99.5%), 10.0 mM TeO_2 (Sigma Aldrich, 99%) and 2.00 M H_2SO_4 (J. T. Baker. ACS Reagent Grade). A 6 mm diameter graphite rod (Sigma Aldrich, 99.995%) was used as the counter electrode. Depositions were conducted for longer times than previously reported

because lengthy depositions under red illumination had previously been shown to promote nodular growth on the lamellae. Shorter deposition times produce minimal secondary growth for red illumination. Nodular growth was deemed desirable because the iridescence of these films arises largely from the presence of nodules on the lamellae.

Growth of samples under pure red and pure blue light showed that the photocurrent density toward deposition of the selenium tellurium film was similar in both cases. Though there was higher photocurrent as measured by the photodiode, the higher external quantum yield for blue illumination made the light current comparable for the two cases. In both cases, the resulting films were highly iridescent. The optical response clearly differed between the two samples, even by visual inspection. The electrodeposition produced films with a glossy, reflective black surface. The structure of the samples was examined microscopically. When examined in an FEI Nova scanning electron microscope using a through lens secondary electron detector, the difference in inter-lamellar spacing in the two samples was apparent. The secondary periodicity of the nodular growths was not visible, however, despite the clear presence of nodule-associated iridescence. When imaged in a Phenom G2 Pro SEM with a backscatter detector in topography mode, humps along the surface of the lamellae could be identified. The deposition conditions used produced subtle nodular growth on the lamellae, though that subtle growth is apparently sufficient to cause appreciable diffraction.

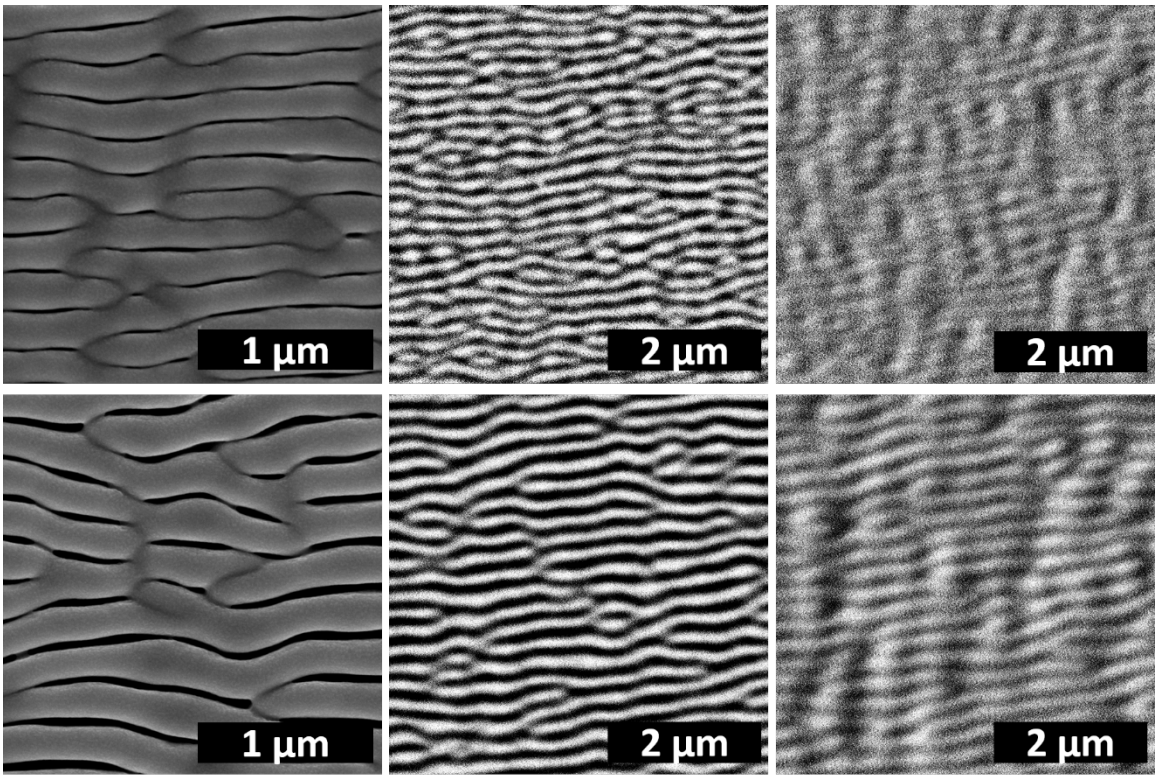

Figure 28: Morphology of Films Deposited under Projector Illumination

The samples on the top row were grown using pure blue light from the projector. The samples on the bottom used pure red light. From left to right, the images are 100,000x magnification micrographs using a secondary electron detector, 45,000x magnification micrographs using a backscatter detector, and 45,000x magnification micrographs using a backscatter detector in topography mode. Subtle nodular growth is apparent in the far right images.

Patterning electrodes with a spatially varying lamellar structure was performed by projecting a two tone image, in this case a (0,0,255) blue Caltech “C” logo on a (255,0,0) red background. Red and blue were chosen because the films associated with each color of illumination would be as distinct as possible given the illumination sources available in the projector. As before, finished electrodes had a reflective black finish, with the “C” logo barely visible. One sample was coated with a thin aluminum coating to enhance reflectivity. The aluminum coating was deposited in a metal evaporator at a base pressure $< 10^{-5}$ Torr. A 20 nm reflective layer of aluminum (Kurt J. Lesker Company, 99.999%) was deposited *via* electron beam evaporation at 10 kV accelerating voltage and 40 mA emission current. The metal coated electrode with the “C” logo had a mirror-like finish. The “C” portion of the electrode was slightly darker, possibly due to more light being diffracted and less light undergoing specular reflection. Under SEM, the pitch of the lamellae differed in the regions grown under red illumination versus regions illuminated with blue light during deposition.

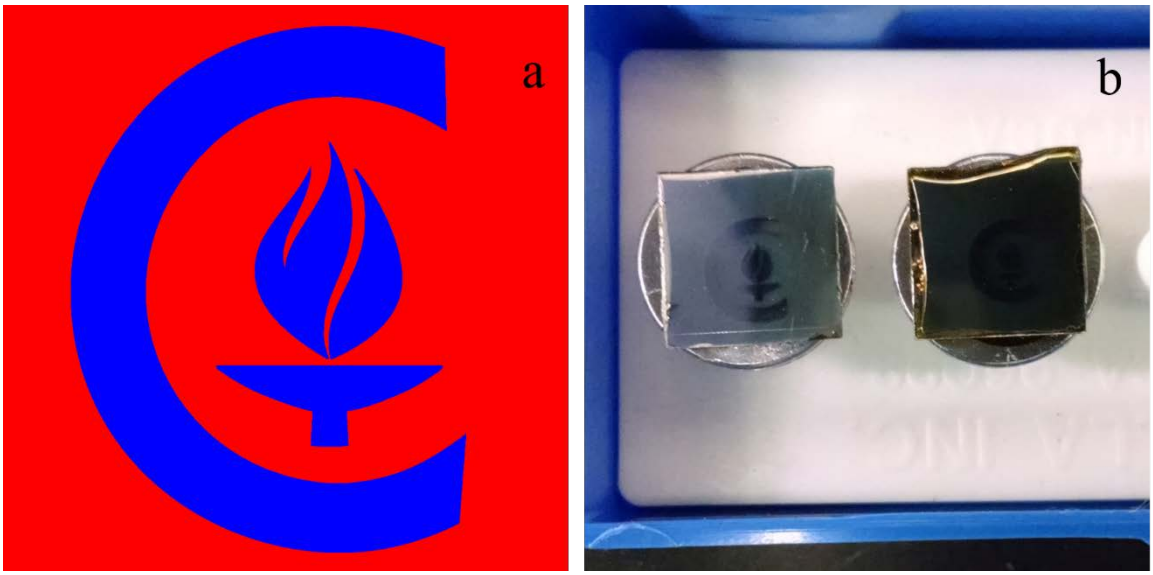

Figure 29: Patterning with a Projected Image

(a) The Caltech icon converted to blue and red. This image was centered in a red background and projected onto electrodes to create a spatially varying nanoscale surface structure. (b) Two electrodes patterned with self-structuring selenium tellurium films under projector illumination. The sample on the left has been coated with aluminum, while the sample on the right is bare selenium tellurium. The “C” and torch are clearly visible on the metalized electrode. The pattern is only just visible on the bare electrode.

The utility of these coatings for coloration was examined by illuminating the samples with broadband light and photographing the samples. An ELH halogen lamp with an equivalent color temperature of 3200 K was used for illumination, and photographs were taken with and Olympus E-PL1 camera. A 60 mm focal length lens was used with an f/16 aperture. The halogen lamp was positioned such that from the sample position, the angle between the camera and the lamp was 63.5°. The sample was then rotated and pictures were taken. The bare selenium tellurium “C” patterned surface showed a continuous variation of background color as the sample was rotated. The inner C and the torch diffracted most strongly at either shallow viewing angles or shallow illumination angles.

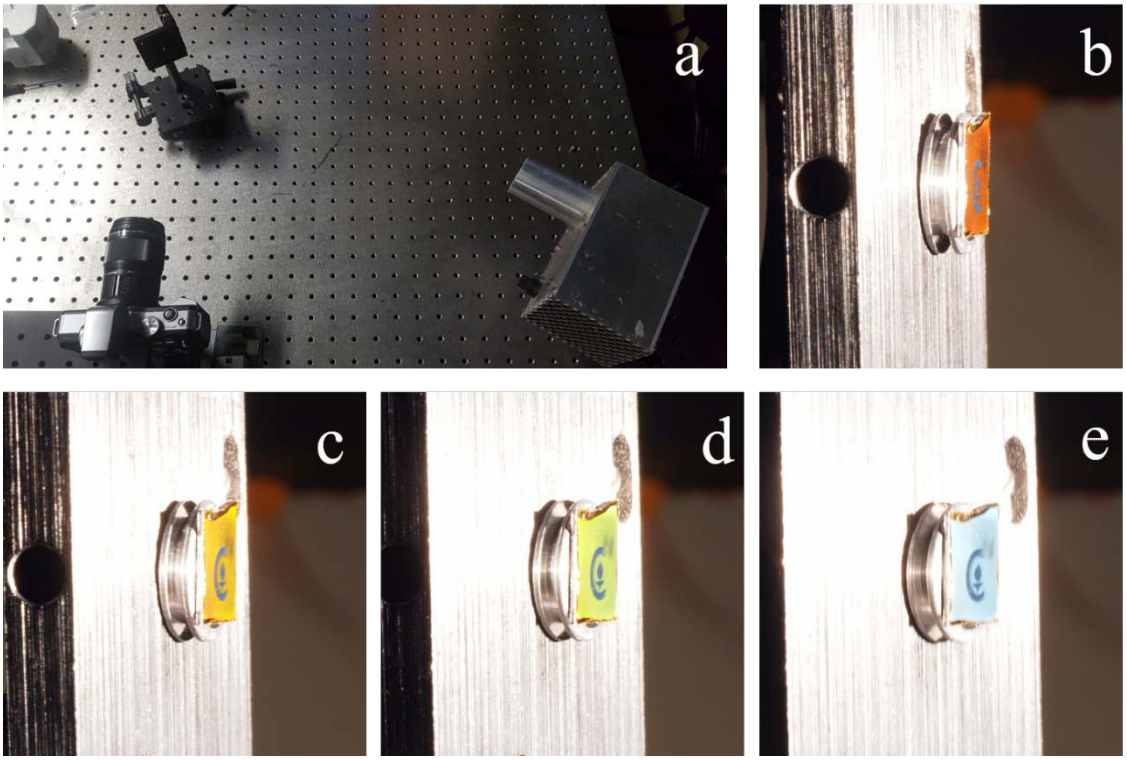

Figure 30: Film Color as a Function of Viewing Angle

(a) The illumination configuration used to assess the iridescence of the patterned films. (b) The bare electrode viewed at an incident angle of 10°. (c) The electrode viewed at 15°. (d) The electrode viewed at 20° (e) the electrode viewed at 25°.

The previous experiment was repeated with the aluminized sample patterned with a Caltech logo. The results were similar to those with the uncoated selenium tellurium sample. The region grown under blue illumination was most colorful at the shallowest illumination or viewing angles. The C portion of the aluminized electrode had a slightly greener cast than seen in the bare sample. There was occasionally disagreement between the photographed color and the viewed color. The white background in the photographs looked greener in person, and the blue-green “C” at glancing angles appeared more aquamarine.

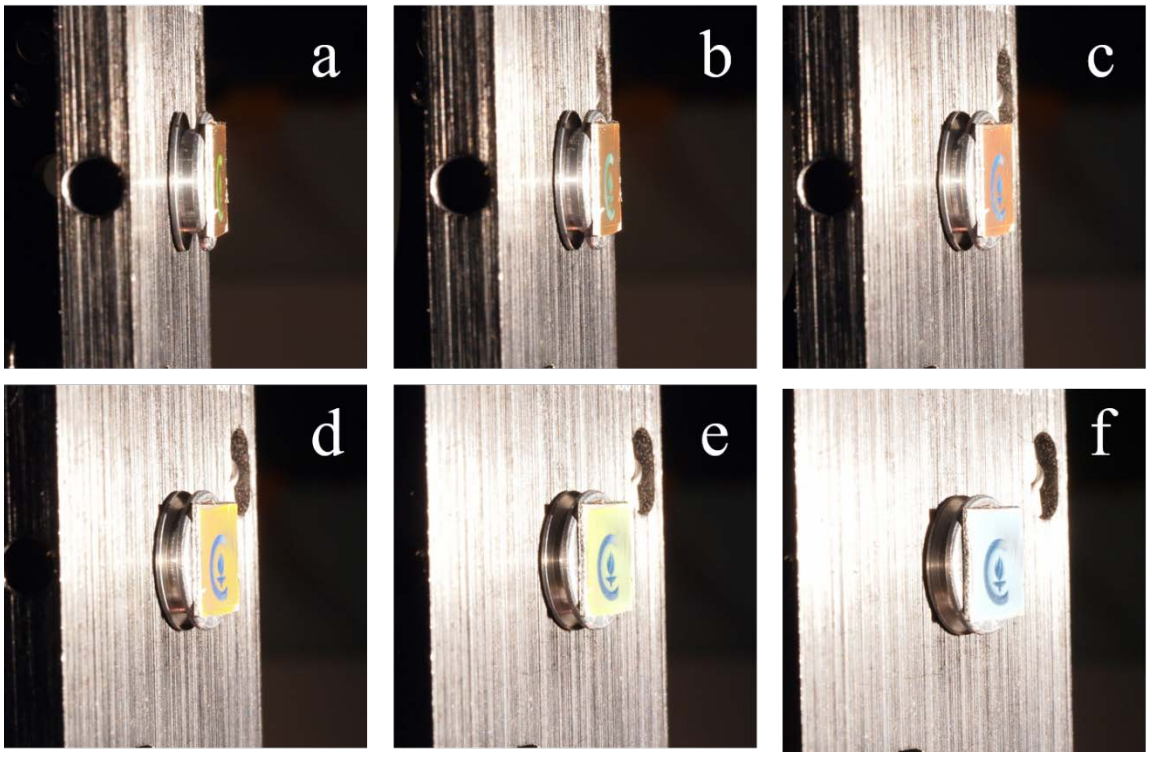

Figure 31: Film Color of Aluminized Sample as a Function of Viewing Angle

(a) The aluminized electrode viewed at an incident angle of 5°. (b) The electrode viewed at an angle of 10°. (c) The electrode viewed at 15°. (d) The electrode viewed at 20°. (e) The electrode viewed at 25°. (f) The electrode viewed at 30°.

Because the color produced by these structures depends on both viewing angle and illumination angle, these experiments were repeated with the halogen lamp relocated. The halogen lamp was moved as close to the camera as possible for the following images. The lamp was slightly to the left of the camera. The angle formed between the lamp and the camera at the sample was 15.5° in this arrangement. When the aluminized sample was both illuminated and photographed from a glancing angle, the region illuminated with blue light during deposition lit up while the area grown under red illumination remained gray. The wavelength of the light diffracted back to the camera shifted continuously from red to blue as the sample was rotated. Only at near normal incidence did the background take on color. The background turns yellow and then orange as the illumination approached normal incidence. The background likely turned red, but the mirror finish on the sample caused all diffraction to be washed out by specular white light when very close to normal incidence.

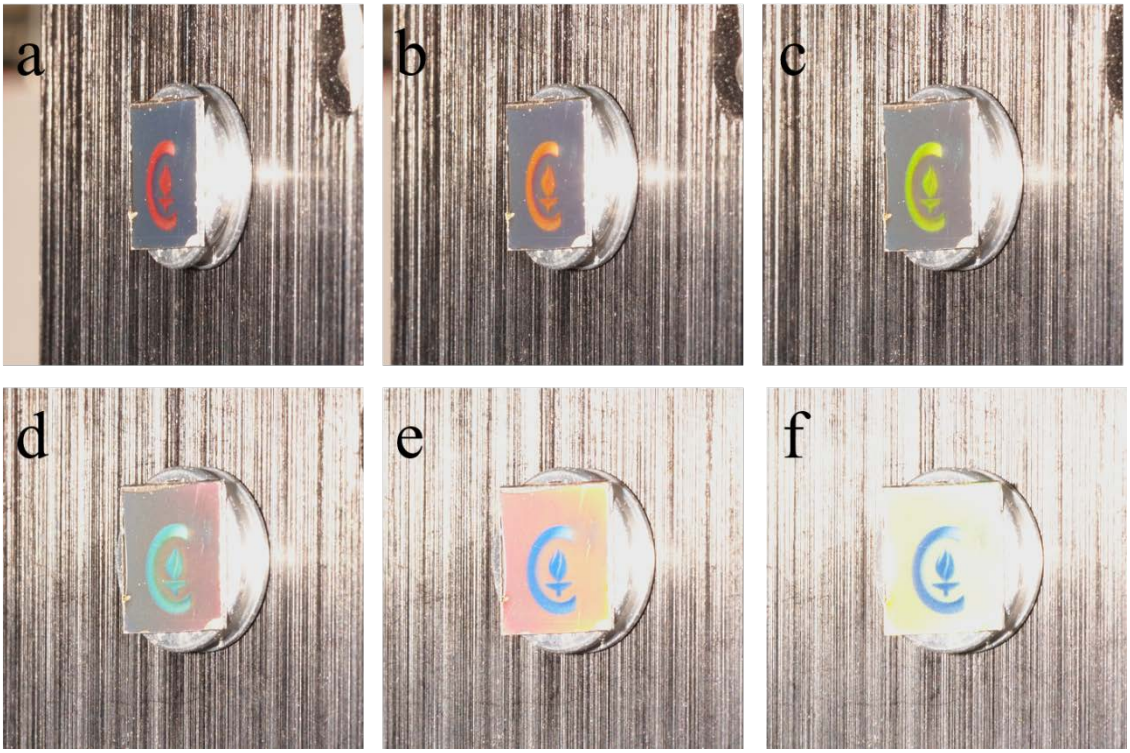

Figure 32: Film Color as a Function of Viewing Angle near Normal Incidence

(a) The aluminized electrode viewed at an incident angle of 30°. (b) The electrode viewed at an angle of 35°. (c) The electrode viewed at 40°. (d) The electrode viewed at 45°. (e) The electrode viewed at 50°. (f) The electrode viewed at 55°.

Diffraction off the lamellae, as opposed to the nodules, was also considered. The sample was rotated 90° and the previous experiment was repeated. The background turned a shade of blue very similar to that seen in *Morpho* butterflies. The sample remained blue at a wide range of angles. At no point did its color shift to longer wavelengths. Diffraction gratings are incapable of diffracting light of a wavelength greater than twice the period of the surface features. Further, for wavelengths near this cutoff, light would be diffracted at glancing angles at normal illumination, so no long wavelength light would be diffracted into the camera. The “C” portion of the electrode, which has a smaller period than the background, only showed deep purple coloration for the same reason.

Figure 33: Angle Dependent Iridescence Derived from Lamellar Period

(a) The aluminized electrode viewed at an incident angle of 10°. (b) The electrode viewed at an angle of 15°. (c) The electrode viewed at 20°. (d) The electrode viewed at 25°. (e) The electrode viewed at 30°. (f) The electrode viewed at 35°.

4.4 Conclusions

The experiments described herein constitute a thorough, but by no means exhaustive, investigation of the optical diffraction from the surface of spontaneously structuring photoelectrodeposited semiconductor alloys. The origin of the coloration has been identified as diffraction as governed by the grating equation. The diffraction of incident light to a diffuse spot prompted comparisons to structural coloration found in nature. Structural color was successfully derived from both the nodular periods and the lamellar periods. Samples were fabricated where illumination was varied spatially to produce arbitrary iridescent designs on a 1 cm by 1 cm square, suggesting that these structures could be used to create structural color economically on large scales.

Future investigators of the optical properties of these systems have many interesting avenues available to them. The patterning was done with only two of the colors the projector could produce for simplicity. By using green as well, substantially more complicated patterns could be produced. Additionally, combinations of blue and green light show promise for creating microscopic surface morphologies with continuously variable pitches. If arbitrarily tunable surface morphologies can be realized synthetically, films could be deposited to diffract a specific wavelength of light at a given set of illumination conditions. One could then, in principle, design an illumination pattern that would result in the deposition of an electrode surface capable of producing an arbitrary color image when illuminated and viewed in a specific manner. Finally, the electrode size was constrained to a 1 cm by 1 cm by the electrochemical cell available for the deposition and, to a lesser extent, by the power of the

projector. With a specially designed cell and a more powerful projector, facile patterning of wafer scale structural coloration would be possible.

BIBLIOGRAPHY

1. Annual Semiconductor Sales Increase 21.6 Percent, Top $400 Billion for First Time. Available at: https://www.semiconductors.org/news/2018/02/05/global_sales_report_2017/annual_semiconductor_sales_increase_21.6_percent_top_400_billion_for_first_time//. (Accessed: 24th May 2018)
2. Robert Bogue. Recent developments in MEMS sensors: a review of applications, markets and technologies. *Sens. Rev.* **33,** 300–304 (2013).
3. Judy, J. W. Microelectromechanical systems (MEMS): fabrication, design and applications. *Smart Mater. Struct.* **10,** 1115 (2001).
4. LaPedus, M. EUV tool costs hit $120 million. *EETimes* Available at: https://www.eetimes.com/document.asp?doc_id=1257963. (Accessed: 24th May 2018)
5. About the ALS. *ALS* Available at: https://als.lbl.gov/about/about-the-als/. (Accessed: 24th May 2018)
6. Haynes, C. L. & Van Duyne, R. P. Nanosphere Lithography: A Versatile Nanofabrication Tool for Studies of Size-Dependent Nanoparticle Optics. *J. Phys. Chem. B* **105,** 5599–5611 (2001).
7. Bowden, N., Brittain, S., Evans, A. G., Hutchinson, J. W. & Whitesides, G. M. Spontaneous formation of ordered structures in thin films of metals supported on an elastomeric polymer. **393,** 4 (1998).

8. Kim, H. C., Kim, D. H. & Chun, K. Photo-assisted electrochemical etching of a nano-gap trench with high aspect ratio for MEMS applications. *J. Micromechanics Microengineering* **16,** 906 (2006).

9. Wagner, L., Ross, I., Foster, J. & Hankamer, B. Trading Off Global Fuel Supply, CO2 Emissions and Sustainable Development. *PLOS ONE* **11,** e0149406 (2016).

10. Friedlingstein, P. *et al.* Persistent growth of CO_2 emissions and implications for reaching climate targets. *Nat. Geosci.* **7,** 709–715 (2014).

11. Collins, M. *et al.* The impact of global warming on the tropical Pacific Ocean and El Niño. *Nat. Geosci.* **3,** 391–397 (2010).

12. Jacobson, M. Z. Review of solutions to global warming, air pollution, and energy security. *Energy Env. Sci* **2,** 148–173 (2009).

13. Dai, A. Drought under global warming: a review. *Wiley Interdiscip. Rev. Clim. Change* **2,** 45–65

14. Ardo, S., Park, S. H., Warren, E. L. & Lewis, N. S. Unassisted solar-driven photoelectrosynthetic HI splitting using membrane-embedded Si microwire arrays. *Energy Environ. Sci.* **8,** 1484–1492 (2015).

15. Audesirk, H. A., Warren, E. L., Ku, J. & Lewis, N. S. Ordered Silicon Microwire Arrays Grown from Substrates Patterned Using Imprint Lithography and Electrodeposition. *ACS Appl. Mater. Interfaces* **7,** 1396–1400 (2015).

16. Roske, C. W. *et al.* Comparison of the Performance of CoP-Coated and Pt-Coated Radial Junction n+p-Silicon Microwire-Array Photocathodes for the Sunlight-Driven Reduction of Water to H2(g). *J. Phys. Chem. Lett.* **6,** 1679–1683 (2015).

17. Shaner, M. R., McDowell, M. T., Pien, A., Atwater, H. A. & Lewis, N. S. Si/TiO2 Tandem-Junction Microwire Arrays for Unassisted Solar-Driven Water Splitting. *J. Electrochem. Soc.* **163,** H261–H264 (2016).

18. Shaner, M. R. *et al.* Photoelectrochemistry of core–shell tandem junction n–p+-Si/n-WO3 microwire array photoelectrodes. *Energy Environ. Sci.* **7,** 779–790 (2014).

19. Yalamanchili, S. *et al.* Enhanced Absorption and <1% Spectrum-and-Angle-Averaged Reflection in Tapered Microwire Arrays. *ACS Photonics* **3,** 1854–1861 (2016).

20. Warren, E. L., Atwater, H. A. & Lewis, N. S. Silicon Microwire Arrays for Solar Energy-Conversion Applications. *J. Phys. Chem. C* **118,** 747–759 (2014).

21. M. Collins, S., M. Hankett, J., I. Carim, A. & Maldonado, S. Preparation of photoactive ZnGeP 2 nanowire films. *J. Mater. Chem.* **22,** 6613–6622 (2012).

22. Putnam, M. C. *et al.* Si microwire-array solar cells. *Energy Environ. Sci.* **3,** 1037–1041 (2010).

23. Waleed, A. *et al.* All Inorganic Cesium Lead Iodide Perovskite Nanowires with Stabilized Cubic Phase at Room Temperature and Nanowire Array-Based Photodetectors. *Nano Lett.* **17,** 4951–4957 (2017).

24. Greene, L. E., Yuhas, B. D., Law, M., Zitoun, D. & Yang, P. Solution-Grown Zinc Oxide Nanowires. *Inorg. Chem.* **45,** 7535–7543 (2006).

25. Bandaranayake, R. J., Wen, G. W., Lin, J. Y., Jiang, H. X. & Sorensen, C. M. Structural phase behavior in II–VI semiconductor nanoparticles. *Appl. Phys. Lett.* **67,** 831–833 (1995).

26. Beberwyck, B. J. & Alivisatos, A. P. Ion Exchange Synthesis of III–V Nanocrystals. *J. Am. Chem. Soc.* **134,** 19977–19980 (2012).

27. Liu, P. *et al.* Organic–Inorganic Hybrid Perovskite Nanowire Laser Arrays. *ACS Nano* **11,** 5766–5773 (2017).

28. Zhu, H. *et al.* Lead halide perovskite nanowire lasers with low lasing thresholds and high quality factors. *Nat. Mater.* **14,** 636–642 (2015).

29. Grzelczak, M., Vermant, J., Furst, E. M. & Liz-Marzán, L. M. Directed Self-Assembly of Nanoparticles. *ACS Nano* **4,** 3591–3605 (2010).

30. Boal, A. K. *et al.* Self-assembly of nanoparticles into structured spherical and network aggregates. *Nature* **404,** 746–748 (2000).

31. Kotov, N. A. & Weiss, P. S. Self-Assembly of Nanoparticles: A Snapshot. *ACS Nano* **8,** 3101–3103 (2014).

32. Rabani, E., Reichman, D. R., Geissler, P. L. & Brus, L. E. Drying-mediated self-assembly of nanoparticles. *Nature* **426,** 271–274 (2003).

33. Zeng, H., Li, J., Liu, J. P., Wang, Z. L. & Sun, S. Exchange-coupled nanocomposite magnets by nanoparticle self-assembly. *Nature* **420,** 395–398 (2002).

34. Zhang, Horsch, M. A., Lamm, M. H. & Glotzer, S. C. Tethered Nano Building Blocks: Toward a Conceptual Framework for Nanoparticle Self-Assembly. *Nano Lett.* **3,** 1341–1346 (2003).

35. Beardslee, J. A., Sadtler, B. & Lewis, N. S. Magnetic Field Alignment of Randomly Oriented, High Aspect Ratio Silicon Microwires into Vertically Oriented Arrays. *ACS Nano* **6,** 10303–10310 (2012).

36. Hughes, M. L. & Dougan, L. The physics of pulling polyproteins: a review of single molecule force spectroscopy using the AFM to study protein unfolding. *Rep. Prog. Phys.* **79,** 076601 (2016).

37. Grohmann, S., Rothe, H., Frant, M. & Liefeith, K. Colloidal Force Spectroscopy and Cell Biological Investigations on Biomimetic Polyelectrolyte Multilayer Coatings Composed of Chondroitin Sulfate and Heparin. *Biomacromolecules* **12,** 1987–1997 (2011).

38. Chung, K.-H., Shaw, G. A. & Pratt, J. R. Accurate noncontact calibration of colloidal probe sensitivities in atomic force microscopy. *Rev. Sci. Instrum.* **80,** 065107 (2009).

39. The Colloidal Probe Technique and its Application to Adhesion Force Measurements - Kappl - 2002 - Particle & Particle Systems Characterization - Wiley Online Library. Available at: https://onlinelibrary-wiley-com.clsproxy.library.caltech.edu/doi/abs/10.1002/1521-4117%28200207%2919%3A3%3C129%3A%3AAID-PPSC129%3E3.0.CO%3B2-G. (Accessed: 25th May 2018)

40. Sedin, D. L. & Rowlen, K. L. Adhesion Forces Measured by Atomic Force Microscopy in Humid Air. *Anal. Chem.* **72,** 2183–2189 (2000).

41. Israelachvili, J. N. *Intermolecular and surface forces*. (Academic Press, 2011).

42. Griffiths, D. J. *Introduction to electrodynamics*. (Prentice Hall, 1999).

43. Gallant, B. M., Gu, X. W., Chen, D. Z., Greer, J. R. & Lewis, N. S. Tailoring of Interfacial Mechanical Shear Strength by Surface Chemical Modification of Silicon Microwires Embedded in Nafion Membranes. *ACS Nano* **9,** 5143–5153 (2015).

44. Sulpizi, M., Gaigeot, M.-P. & Sprik, M. The Silica-Water Interface: How the Silanols Determine the Surface Acidity and Modulate the Water Properties. *J. Chem. Theory Comput.* **8,** 1037–1047 (2012).

45. Bard, A. J. & Faulkner, L. R. *Electrochemical methods: fundamentals and applications*. (Wiley, 1980).

46. Rock, P. A. The Standard Oxidation Potential of the Ferrocyanide-Ferricyanide Electrode at 25° and the Entropy of Ferrocyanide Ion. *J. Phys. Chem.* **70,** 576–580 (1966).

47. THOMPSON, L. F. An Introduction to Lithography. in *Introduction to Microlithography* **219,** 1–13 (AMERICAN CHEMICAL SOCIETY, 1983).

48. Poulsen, R. G. Plasma etching in integrated circuit manufacture—A review. *J. Vac. Sci. Technol.* **14,** 266–274 (1977).

49. Elwenspoek, M. & Jansen, H. *Silicon micromachining*. (Cambridge University Press, 1998).

50. Williams, K. R., Gupta, K. & Wasilik, M. Etch rates for micromachining processing-part II. *J. Microelectromechanical Syst.* **12,** 761–778 (2003).

51. Williams, K. R. & Muller, R. S. Etch rates for micromachining processing. *J. Microelectromechanical Syst.* **5,** 256–269 (1996).

52. Kovacs, G. T. A., Maluf, N. I., Kurt & Petersen, E. Bulk micromachining of silicon. in *Proc. IEEE* 1536–1551 (1998).

53. Zhao, L. *et al.* Porous Silicon and Alumina as Chemically Reactive Templates for the Synthesis of Tubes and Wires of SnSe, Sn, and SnO2. *Angew. Chem. Int. Ed.* **45,** 311–315

54. Dalisa, A. L., Zwicker, W. K., DeBitetto, D. J. & Harnack, P. Photoanodic engraving of holograms on silicon. *Appl. Phys. Lett.* **17,** 208–210 (1970).

55. Matthias, S., Müller, F., Jamois, C., Wehrspohn, R. B. & Gösele, U. Large-Area Three-Dimensional Structuring by Electrochemical Etching and Lithography. *Adv. Mater.* **16,** 2166–2170

56. Birner, A., Wehrspohn, R. B., Gösele, U. M. & Busch, K. Silicon-Based Photonic Crystals. *Adv. Mater.* **13,** 377–388

57. Sadtler, B. *et al.* Phototropic growth control of nanoscale pattern formation in photoelectrodeposited Se–Te films. *Proc. Natl. Acad. Sci.* **110,** 19707–19712 (2013).

58. Carim, A. I., Batara, N. A., Premkumar, A., Atwater, H. A. & Lewis, N. S. Self-Optimizing Photoelectrochemical Growth of Nanopatterned Se–Te Films in Response to the Spectral Distribution of Incident Illumination. (2015). doi:10.1021/acs.nanolett.5b03137

59. Carim, A. I. *et al.* Morphological Expression of the Coherence and Relative Phase of Optical Inputs to the Photoelectrodeposition of Nanopatterned Se–Te Films. *Nano Lett.* **16,** 2963–2968 (2016).

60. Carim, A. I., Batara, N. A., Premkumar, A., Atwater, H. A. & Lewis, N. S. Polarization Control of Morphological Pattern Orientation During Light-Mediated Synthesis of Nanostructured Se–Te Films. (2015). doi:10.1021/acsnano.5b05119

61. Carim, A. I. *et al.* Template-Free Synthesis of Periodic Three-Dimensional PbSe Nanostructures via Photoelectrodeposition. *J. Am. Chem. Soc.* (2018). doi:10.1021/jacs.8b02931

62. Development of structural colour in leaf beetles | Scientific Reports. Available at: https://www-nature-com.clsproxy.library.caltech.edu/articles/s41598-017-01496-8. (Accessed: 25th May 2018)

63. Vignolini, S. *et al.* Pointillist structural color in Pollia fruit. *Proc. Natl. Acad. Sci. U. S. A.* **109,** 15712–15715 (2012).

64. KINOSHITA, S., YOSHIOKA, S., FUJII, Y. & OKAMOTO, N. Photophysics of Structural Color in the Morpho Butterflies. 19

65. Feathers, O. T. P., Yoshioka, S. & Kinoshita, S. *Effect of Macroscopic Structure in Iridescent Color.* (2002).

66. Hecht, E. *Optics*. (Addison-Wesley, 2002).

67. Gümrah Dumanli, A. & Savin, T. Recent advances in the biomimicry of structural colours. *Chem. Soc. Rev.* **45,** 6698–6724 (2016).

68. Hedayati, M. K. & Elbahri, M. Review of Metasurface Plasmonic Structural Color. *Plasmonics* **12,** 1463–1479 (2017).

69. Kinoshita, S., Yoshioka, S. & Miyazaki, J. Physics of structural colors. *Rep. Prog. Phys.* **71,** 076401 (2008).

70. Zhao, Y. *et al.* Artificial Structural Color Pixels: A Review. *Mater. Basel Switz.* **10,** (2017).

71. Boyle, B. M., French, T. A., Pearson, R. M., McCarthy, B. G. & Miyake, G. M. Structural Color for Additive Manufacturing: 3D-Printed Photonic Crystals from Block Copolymers. *ACS Nano* **11,** 3052–3058 (2017).

72. Wu, Y.-K. R., Hollowell, A. E., Zhang, C. & Guo, L. J. Angle-Insensitive Structural Colours based on Metallic Nanocavities and Coloured Pixels beyond the Diffraction Limit. *Sci. Rep.* **3,** 1194 (2013).

73. Kanamori, Y., Shimono, M. & Hane, K. Fabrication of Transmission Color Filters Using Silicon Subwavelength Gratings on Quartz Substrates. *IEEE Photonics Technol. Lett.* **18,** 2126–2128 (2006).

74. Aguirre, C. I., Reguera, E. & Stein, A. Tunable Colors in Opals and Inverse Opal Photonic Crystals. *Adv. Funct. Mater.* **20,** 2565–2578

75. Lee, H. S. *et al.* Photonic properties of titania inverse opal heterostructures. *Opt. Mater. Express* **3,** 1007–1019 (2013).

76. Liu, F., Shan, B., Zhang, S. & Tang, B. SnO $_2$ Inverse Opal Composite Film with Low-Angle-Dependent Structural Color and Enhanced Mechanical Strength. *Langmuir* **34,** 3918–3924 (2018).

77. Peng, S. *et al.* Three-dimensional single gyroid photonic crystals with a mid-infrared bandgap. *ArXiv160403675 Phys.* (2016).

78. Chernow, V. F., Alaeian, H., Dionne, J. A. & Greer, J. R. Polymer lattices as mechanically tunable 3-dimensional photonic crystals operating in the infrared. *Appl. Phys. Lett.* **107,** 101905 (2015).

79. Hutley, M. C. Interference (holographic) diffraction gratings. *J. Phys. [E]* **9,** 513 (1976).

80. Klein, M. V. & Furtak, T. E. *Optics*. (Wiley, 1986).

81. Ding, Y., Xu, S. & Wang, Z. L. (Zhong L. Structural colors from Morpho peleides butterfly wing scales. (2009).

82. Smith, G. S. Structural color of Morpho butterflies. *Am. J. Phys.* **77,** 1010–1019 (2009).

83. Kinoshita, S., Yoshioka, S. & Kawagoe, K. Mechanisms of structural colour in the Morpho butterfly: cooperation of regularity and irregularity in an iridescent scale. *Proc. R. Soc. B Biol. Sci.* **269,** 1417–1421 (2002).

84. Zhang, S. & Chen, Y. Nanofabrication and coloration study of artificial *Morpho* butterfly wings with aligned lamellae layers. *Sci. Rep.* **5,** 16637 (2015).